

See discussions, stats, and author profiles for this publication at: <https://www.researchgate.net/publication/260631645>

A solid-shell corotational element based on ANDES, ANS and EAS for geometrically nonlinear structural analysis

Article in *International Journal for Numerical Methods in Engineering* · July 2013

DOI: 10.1002/nme.4504

CITATIONS

54

READS

1,193

3 authors:



Mohammadreza Mostafa

University of Colorado Boulder

6 PUBLICATIONS 99 CITATIONS

[SEE PROFILE](#)



Mettupalayam Sivaselvan

University at Buffalo, The State University of New York

87 PUBLICATIONS 2,027 CITATIONS

[SEE PROFILE](#)



Carlos Felippa

University of Colorado Boulder

209 PUBLICATIONS 7,664 CITATIONS

[SEE PROFILE](#)

Some of the authors of this publication are also working on these related projects:



Aplicação de elementos finitos de sólidos 3D de baixa ordem e da formulação corotacional na análise inelástica de placas e lâminas [View project](#)



Transforming online books to physical ones. [View project](#)

A solid-shell corotational element based on ANDES, ANS and EAS for geometrically nonlinear structural analysis

M. Mostafa¹, M. V. Sivaselvan^{2,*} and C. A. Felippa³

¹*Department of Civil, Environmental and Architectural Engineering, University of Colorado at Boulder, Boulder, CO 80309, USA*

²*Department of Civil, Structural and Environmental Engineering, University at Buffalo, Buffalo, NY 14221, USA*

³*Department of Aerospace Engineering Sciences and Center for Aerospace Structures, University of Colorado at Boulder, Boulder, CO 80309, USA*

SUMMARY

This paper describes an eight-node, assumed strain, solid-shell, corotational element for geometrically nonlinear structural analysis. The locally linear kinematics of the element is separated into in-plane (which is further decoupled into membrane and bending), thickness and transverse shear components. This separation allows using any type of membrane quadrilateral formulation for the in-plane response. Assumed strain fields for the three components are constructed using different approaches. The Assumed Natural Deviatoric Strain approach is used for the in-plane response, whereas the Assumed Natural Strain approach is used for the thickness and transverse shear components. A strain enhancement based on Enhanced Assumed Strain concepts is also used for the thickness component. The resulting element passes well-known shell element patch tests and exhibits good performance in a number of challenging benchmark tests. The formulation is extended to the geometric nonlinear regime using an element-independent corotational approach. Some key properties of the corotational kinematic description are discussed. The element is tested in several well-known shell benchmarks and compared with other thin-shell and solid-shell elements available in the literature, as well as with commercial nonlinear FEM codes. Copyright © 2013 John Wiley & Sons, Ltd.

Received 29 September 2012; Revised 12 March 2013; Accepted 21 March 2013

KEY WORDS: solid shell; ANDES; ANS; EAS; corotational

1. INTRODUCTION

Shell finite elements are commonly used to model three-dimensional (3D) structures in which the extent in one direction (referred to as the thickness direction in the sequel) is much smaller than in the other two directions. Shell elements may be classified into three broad categories – (i) classical shell elements, (ii) degenerate shell elements and (iii) solid-shell elements. Classical shell elements are based on the conventional theories of plates and shells, and have nodes with rotational DOF [1–5]. Degenerated shell elements start from the continuum theory but impose appropriate constraints to express the kinematics in terms of the shell mid-surface state [6–12]. These elements also have nodes with rotational DOF. Solid-shell elements resemble solid elements in that their nodes, which are located on the top and bottom surfaces, possess only translational DOF. For these, special measures must be taken to overcome problems arising from the thickness being much smaller than the other two spatial dimensions. Buechter and Ramm [13] discuss the difference between classical

*Correspondence to: M. V. Sivaselvan, Department of Civil, Structural and Environmental Engineering, University at Buffalo, Buffalo, NY 14221, USA.

†E-mail: mvs@buffalo.edu

and degenerate shell formulations. A paradigm for thin-shell elements that falls outside the aforementioned three categories is based on the concept of subdivision surfaces [14, 15] and has been found to outperform traditional formulations.

In this paper, a solid-shell formulation is developed using an assumed strain approach. Attractive features of a solid-shell element include the following.

- Modeling simplifications that result from avoiding 3D rotational DOF (in fact, this work was motivated by a model reduction application, in which the element configuration space with only translational DOF has a simpler vector space structure).
- Realistic representation of 3D boundary conditions without need for additional kinematic assumptions. For example, distinctions can be made as to whether supports are applied to the top or bottom surface.
- Simplified coupling with standard solid elements without multifreedom constraints. This coupling may be necessary when smooth shell structures interact with features that require a more detailed 3D treatment, such as folds, edge reinforcements or mushroom slab supports.

Examples of early work on solid-shell elements are addressed in [16–19]. Sze [20] discussed the different challenges that arise in solid-shell element development and strategies that have been developed to address them. Schwarze and Reese [21] present a comprehensive survey of different solid-shell element formulations.

In modeling shell structures, the well-known displacement-based approach used in conventional solid elements is not rich enough to capture kinematics associated with bending normal to the shell surface. As a result, solid-shell elements are susceptible to several kinds of locking phenomena:

- *Membrane locking* is triggered when the element is subjected to in-plane longitudinal or transverse shear loads and low-order shape functions are incapable of capturing the correct in-plane bending response. This behavior is exacerbated by element in-plane distortion as well as high aspect ratios.
- *Transverse shear locking* occurs when the element thickness tends to zero or, equivalently, the element has high aspect ratio in terms of length versus thickness. The Enhanced Assumed Strain (EAS) approach has been effective in reducing the effect of parasitic shear terms, see [22, 23] for small strains and [24, 25] for large strains. Another remedy is the Assumed Natural Strain (ANS) approach, see [18, 21, 26–31] for solid-shell elements.
- *Poisson thickness locking* occurs when the across-the-thickness displacement is assumed to vary linearly, whence the thickness strain becomes constant. However, because of Poisson's ratio effect, that strain couples with in-plane strains that do vary linearly across the thickness. This discrepancy results in locking. Remedies include the following: assuming a quadratic displacement variation along the thickness direction [16]; using EAS DOSs thus enhancing the thickness strain to vary linearly [21]; or splitting the thickness strain into membrane (constant) and bending (linear) parts, and enforcing the bending stress to be zero [18].
- *Curvature or trapezoidal locking* occurs when the element edges in the thickness direction are not perpendicular to the element mid-plane. This happens in modeling curved shells with thickness tapered solid-shell elements. The ANS concept has been shown to circumvent this defect, as can be found in [2, 21, 32].

We use several variants of the assumed strain approach for different components of the solid-shell formulation. Assumed strain finite elements were first used by MacNeal [33] in 1978. Several variations of this idea evolved over the following two decades. The ANS variant was introduced by Park and Stanley [8] for doubly curved thin shells. A related technique, labeled mixed interpolation of tensorial components (MITC), was developed by Bathe and Dvorkin [7, 34] for flat elements. The Assumed Natural Deviatoric Strain (ANDES) variant of Felippa and Militello [35, 36] represents a combination of the Free Formulation (FF) of Bergan [37–41] and of ANS. A variational framework was presented by Simo and Hughes [42], which eventually evolved into the EAS variant.

The kinematics of the solid-shell element presented here is decomposed into in-plane, transverse shear and thickness components. The in-plane behavior is handled by ANDES, an approach that helps alleviate membrane locking. ANS fields are constructed for the out-of-plane components,

that is, transverse shear and thickness components, by computing compatible strains at collocation points and interpolating these strains. This approach mitigates transverse shear locking and curvature locking. The thickness strain is enhanced to represent linear variation associated with out-of-plane bending, as necessary to avoid Poisson's thickness locking. Full Gauss integration is used in all formulation components guaranteeing correct rank. This combined approach is found to result in accurate numerical solutions in challenging benchmark tests.

The quadrilateral mid-surface of an eight-node solid-shell element is generally warped, that is, its four corners are not necessarily coplanar. Direct application of any interpolation scheme over it may pollute the stiffness with respect to the rigid body modes. That is, rigid motions may produce nonzero in-plane strains, resulting in spurious energy absorption. To circumvent that effect, the projection method introduced in [43] is used.

Various approaches can be found in the literature to formulating solid-shell elements with non-linear kinematics. Only some representative contributions are cited here. Schwarze and Reese [44] developed a reduced-integration geometric nonlinear element based on total Lagrangian kinematics, whereas Abed-Meraim and Combescure [45, 46] used an updated Lagrangian approach. Additional geometrically nonlinear solid-shell formulations include [26, 47–49]. In the current work, the solid-shell element formulation is extended to the geometric nonlinear regime using a corotational (CR) kinematic description. The CR kinematic description was pioneered by Wempner [50] and Belytschko and Hsieh [51]. The CR approach has been widely used on classical shell models, for example in [52–55], as well as continuum-based models, for example in [56, 57]. Among different CR formulations in the literature (see [58] for an historical account of various formulations), the *element-independent corotational* approach, abbreviated to EICR, is used here. This formulation was introduced by Rankin and coworkers [43, 59, 60]. It relies strongly on the use of projection operators.

The EICR scheme is of practical interest because the linear element kernel can be reused for constructing the nonlinear FEM equations. As a result, the element library (which in terms of development and maintenance costs is the most expensive component of large-scale, general-purpose FEM programs) needs not be drastically modified. Although the CR description has been traditionally associated with small deformations but large rotations, some recent extensions to accommodate finite strains have been proposed (e.g., [61]). However, we shall only consider here problems with small strains.

The corotated frame is defined to be independent of whether or not the mid-surface is warped. The element internal force and consistent tangent stiffness matrix are derived by taking variations of the internal energy with respect to its nodal DOF to preserve the *consistency* requirement. Numerical results for the geometrically nonlinear element indicate that this technique works well.

This paper is organized as follows. Section 2 briefly describes the ANDES scheme for the membrane component. Section 3 completes the formulation of the linear solid-shell element. Section 4 covers the treatment of geometric nonlinearity using a CR kinematic description. Section 5 presents numerical examples to evaluate the performance of the present element on a set of linear and geometrically nonlinear benchmark problems. Section 6 summarizes our conclusions.

2. ANDES FORMULATION FOR IN-PLANE RESPONSE

The ANDES formulation was originally proposed for membrane and bending responses of classical thin-shell elements [35, 36, 62]. The concept is to decompose the assumed strain field into the basic modes defined in Cartesian coordinates and higher-order (Deviatoric) modes defined in natural coordinates. The higher-order modes are enforced to be energy orthogonal to the basic modes to guarantee satisfaction of the patch test as an *a priori* requirement in the element development [37]. This notion of energy orthogonality of the higher-order and basic stress modes has been also addressed in [63].

For a plane quadrilateral, the ANDES formulation starts from a two-field variational principle with displacements (u) and strains (e) as independent fields.

$$\begin{aligned} \Pi(u, e) = & \int_V \frac{1}{2} (e - e^u) \cdot E \cdot (e - e^u) dV - \int_V \frac{1}{2} e^u \cdot E \cdot e^u dV \\ & + \int_V b \cdot u dV + \int_{S_t} t^p \cdot u dS \end{aligned} \quad (1)$$

Here, u is the displacement field, e^u is compatible strain field, e is the independent assumed strain field, E matrix representation of the elasticity tensor, S_t is the portion of the domain boundary where tractions are prescribed, b is the body force and t^p is the prescribed traction. For linear elasticity, this can be seen as simply the strain-version of Hellinger–Reissner variational principle [64, 65]. The stationarity conditions of the functional (1) yield

$$\begin{aligned} \int_V (e - e^u) \cdot E \cdot \delta e dV &= 0 \\ \int_V \sigma^e \cdot \delta e^u dV &= \int_V b \cdot \delta u dV + \int_{S_t} t^p \cdot \delta u dS \end{aligned} \quad (2)$$

where $\sigma^e = Ee$ is the strain-derived stress field.

Five strain parameters (χ) are used to approximate the independent strain field. These parameters could be visualized as ‘strain gages’ as shown in Figure 1. χ_1, χ_2, χ_3 at the centroid C represent the constant *cartesian* strains (basic) and χ_4, χ_5 at the edges represent *natural* strains that are interpolated linearly to obtain the bending (higher order) modes. Analogous corresponding fact for assumed stress modes [66], any additional strain gage on the edges will be dependent. The resulting assumed strain field is

$$e(\xi, \eta) = \begin{pmatrix} e_{xx} \\ e_{yy} \\ \gamma_{xy} \end{pmatrix} (\xi, \eta) = \underbrace{\begin{bmatrix} 1 & 0 & 0 & c_m^2(\eta - \eta_c) & c_n^2(\xi - \xi_c) \\ 0 & 1 & 0 & s_m^2(\eta - \eta_c) & s_n^2(\xi - \xi_c) \\ 0 & 0 & 1 & 2c_ms_m(\eta - \eta_c) & 2c_ns_n(\xi - \xi_c) \end{bmatrix}}_{B^n} \begin{pmatrix} \chi_1 \\ \chi_2 \\ \chi_3 \\ \chi_4 \\ \chi_5 \end{pmatrix} \quad (3)$$

(c_m, s_m) and (c_n, s_n) are the direction cosines of the ξ and η axes, and (ξ_c, η_c) the coordinates of the centroid of the element under the isoparametric map (see for example [67]). Substituting (3) and the compatible strain, $e^u(\xi, \eta) = B^{iso}(\xi, \eta)u^Q$, into (2), eliminating the χ parameter from the system

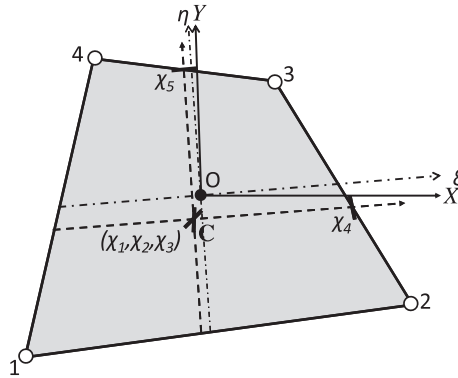


Figure 1. Element response represented by ‘strain gages’ (x, y indicate Cartesian coordinates, ξ, η indicate isoparametric coordinates).

of equations and performing some symbolic calculations yield the following strain-displacement matrix, B^Q , for the ANDES quadrilateral.

$$e(\xi, \eta) = \underbrace{B^n(\xi, \eta) \begin{bmatrix} B^{\text{iso}}(\xi_C, \eta_C) \\ WH_h \end{bmatrix}}_{B^Q(\xi, \eta)} u^e \quad (4)$$

The terms W and H_h are defined in [67]. The detailed derivations related to Equation (4) have been presented in another publication [68]. It can be easily seen that the higher-order modes are energy orthogonal to the basic modes through

$$\int_V (B_h^Q)^T E B_b^Q dV = 0 \quad (5)$$

where, $B_b^Q = B^Q(\xi_C, \eta_C)$ and $B_h^Q = B^Q(\xi, \eta) - B_b^Q$.

In the next section, $B^Q(\xi, \eta)$ in Equation (4) will be used to construct the membrane response of the solid-shell element.

3. LINEAR ELEMENT FORMULATION

This section completes the formulation of a solid-shell element assuming linear kinematics, that is, small deformations and rotations. The element geometry is shown in Figure 2. One of the space directions is identified as the shell-thickness direction. A node-numbering convention is adopted so that edges between nodes (1, 2, 3, 4) and (5, 6, 7, 8), respectively, pertain to the thickness direction. Thus, faces 1–2–3–4 and 5–6–7–8 constitute the bottom and top surfaces of the element, whereas the remaining four faces are *in-plane* surfaces. In formulating the element, it proves convenient to introduce different coordinate systems, which are presented in the paragraphs that follow. Next, a kinematic decomposition of the element behavior is discussed, which motivates the construction of assumed strain fields. This section concludes with the formulation of the complete element stiffness matrix.

We summarize here notational conventions used in the remainder of the paper. Vectors are denoted by boldface letters such as \mathbf{x} . Their components are denoted by medium weight italic letters with appropriate subscripts. Boldface letters with superscript 'e' denote collections of vector components over all element nodes; for the element presented here, such vectors are of length 24. Boldface letters with superscript 'C' denote averages over the nodes of the element; such vectors are of length 3. Boldface letters with other superscripts represent vector components at a specific node or point, the superscript being the label or index of the node or point. Boldface letters with no superscripts

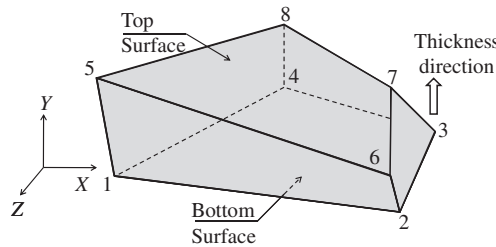


Figure 2. The original solid-shell element of generally warped geometry.

denote vector fields over the element. Matrices and scalars are denoted by italic letters. The following notation for a 3×3 matrix M and a 3-vector \mathbf{v} are found useful in the derivations that follow.

$$\begin{aligned} \text{diag}(M) &= \begin{matrix} & 1 & \dots & n^e \\ \begin{matrix} 1 \\ \vdots \\ n^e \end{matrix} & \begin{bmatrix} M & & \\ & \ddots & \\ & & M \end{bmatrix} \end{matrix}; & \text{array}(M) = \begin{matrix} & 1 & \dots & n^e \\ \begin{matrix} 1 \\ \vdots \\ n^e \end{matrix} & \begin{bmatrix} M & \dots & M \\ \vdots & \ddots & \vdots \\ M & \dots & M \end{bmatrix} \end{matrix}; \\ \text{and } \text{stack}(\mathbf{v}) &= \begin{matrix} & 1 \\ \begin{matrix} 1 \\ \vdots \\ n^e \end{matrix} & \begin{bmatrix} \mathbf{v} \\ \vdots \\ \mathbf{v} \end{bmatrix} \end{matrix} \end{aligned} \quad (6)$$

where n^e is the number of nodes in the element (eight for the solid-shell element presented here) and, in each case, the number of block row and column repetitions is shown on the border. Other specific notation is described as it appears.

3.1. Coordinate systems

In the following, the coordinate systems used in the solid-shell element formulation are presented in order. The base coordinate system in which equilibrium is considered is termed the global coordinate system. Vectors in this coordinate system are denoted by boldface uppercase letters. For example, the position of all the nodes is denoted by \mathbf{X}^e and their displacements by \mathbf{U}^e .

3.1.1. Local coordinate system. First a coordinate system local to the element is constructed. Vectors in this coordinate system are denoted by boldface lowercase letters. The construction of the local coordinate system proceeds as follows.

Construction: Referring to Figure 3, midpoints of edges 1–5, ..., 4–8 are labeled $1^w, \dots, 4^w$ respectively, whereas midpoints of lines $1^w-2^w, \dots, 4^w-1^w$ are labeled $5^0, \dots, 8^0$. The mid-surface $1^w-2^w-3^w-4^w$ is generally warped. However, the lines 5^0-7^0 and 8^0-6^0 do intersect at a point C, whose global coordinates \mathbf{X}^C are given by the average of the nodal coordinates. This point C is chosen as the origin of the local coordinate system. The plane defined by the lines 5^0-7^0 and 8^0-6^0 is taken as the local xy -plane, with its x -direction defined along the line 8^0-6^0 . The local z -direction is normal to this plane. The components in global coordinates of the unit vectors in the local x , y and z directions are thus obtained as[‡]

$$\alpha_x = \frac{\mathbf{X}^{6^0} - \mathbf{X}^{8^0}}{\|\mathbf{X}^{6^0} - \mathbf{X}^{8^0}\|}, \quad \alpha_z = \frac{\alpha_x \times (\mathbf{X}^{7^0} - \mathbf{X}^{5^0})}{\|\alpha_x \times (\mathbf{X}^{7^0} - \mathbf{X}^{5^0})\|}, \quad \alpha_y = \alpha_z \times \alpha_x. \quad (7)$$

The rotation matrix

$$R = [\alpha_x \mid \alpha_y \mid \alpha_z] \quad (8)$$

transforms components of vectors from local coordinates to global coordinates.

We note that any change in node numbering consistent with the scheme described at the beginning of this section can only result in one of two possibilities – the z -axis pointing in the same direction with the x and y axes rotated 180° , or the z -axis pointing in the opposite direction with the x and y axes rotated 90° or 270° . Such a change in node numbering therefore does not affect element behavior.

[‡] α is an exception to the general notation used for vectors – although it is a lowercase character and does not have a superscript, it represents components in global coordinates and is not a vector field over the element.

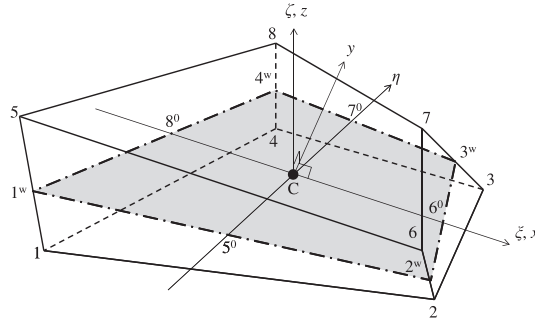


Figure 3. Local and natural coordinate systems.

Transformation of positions and displacements: Node positions and displacements are transformed from global coordinates to local coordinates by

$$\mathbf{x}^n = R^T (\mathbf{X}^n - \mathbf{X}^C), \quad \mathbf{u}^n = R^T \mathbf{U}^n, \quad n = 1, \dots, 8 \quad (9)$$

3.1.2. Natural coordinate system. To approximate displacement and strain fields within the element as carried out in Section 3.2, a natural coordinate system is used, in which region $[-1, 1] \times [-1, 1] \times [-1, 1]$ is mapped to the region occupied by the element. When positions and displacements need to be interpolated, for example, in the computation of compatible strains, the usual isoparametric trilinear shape functions are used. Thus,

$$\mathbf{x}(\xi, \eta, \zeta) = \sum_{n=1}^8 N^n(\xi, \eta, \zeta) \mathbf{x}^n, \quad \mathbf{u}(\xi, \eta, \zeta) = \sum_{n=1}^8 N^n(\xi, \eta, \zeta) \mathbf{u}^n \quad (10)$$

in which $N^n(\xi, \eta, \zeta) = \frac{1}{8}(1 + \xi^n \xi)(1 + \eta^n \eta)(1 + \zeta^n \zeta)$, (ξ^n, η^n, ζ^n) being the natural coordinates of node n . The Jacobian matrix

$$J(\xi, \eta, \zeta) = \begin{bmatrix} \frac{\partial \mathbf{x}}{\partial \xi} & \frac{\partial \mathbf{x}}{\partial \eta} & \frac{\partial \mathbf{x}}{\partial \zeta} \end{bmatrix} \quad (11)$$

is used frequently in the sequel.

3.2. Assumed strain fields

All components of the solid-shell element developed here are formulated using variants of the assumed strain approach. The element kinematics is decomposed into three parts. The assumed strain field in each part is constructed using a different principle.

- *In-plane* deformation: The in-plane assumed strain field is built using the Assumed Natural Deviatoric Strain (ANDES) concept described in Section 2. In turn, the in-plane deformation may be thought of as consisting of *membrane* and *bending* components.
- *Transverse shear* deformation: Assumed transverse shear strains are derived by the ANS approach.
- Deformation in the *thickness* direction: The assumed strain field in the thickness direction is assembled by a combination of the ANS idea and strain enhancement.

The development of the assumed strain field is summarized in Figure 4 and is elaborated in the following. It is noted that besides the use of the assumed strain field, no other techniques such as reduced integration and the ensuing hourglass stabilization etc. are used in the element development.

In terms of notation,

$$\mathbf{e}^C = (e_{xx}, e_{yy}, \gamma_{xy}, e_{zz}, \gamma_{yz}, \gamma_{xz})^T \quad (12)$$

denotes the vector of strain components in the (Cartesian) local coordinate system, and

$$\mathbf{e}^n = (e_{\xi\xi}, e_{\eta\eta}, \gamma_{\xi\eta}, e_{\zeta\zeta}, \gamma_{\eta\zeta}, \gamma_{\xi\zeta})^T \quad (13)$$

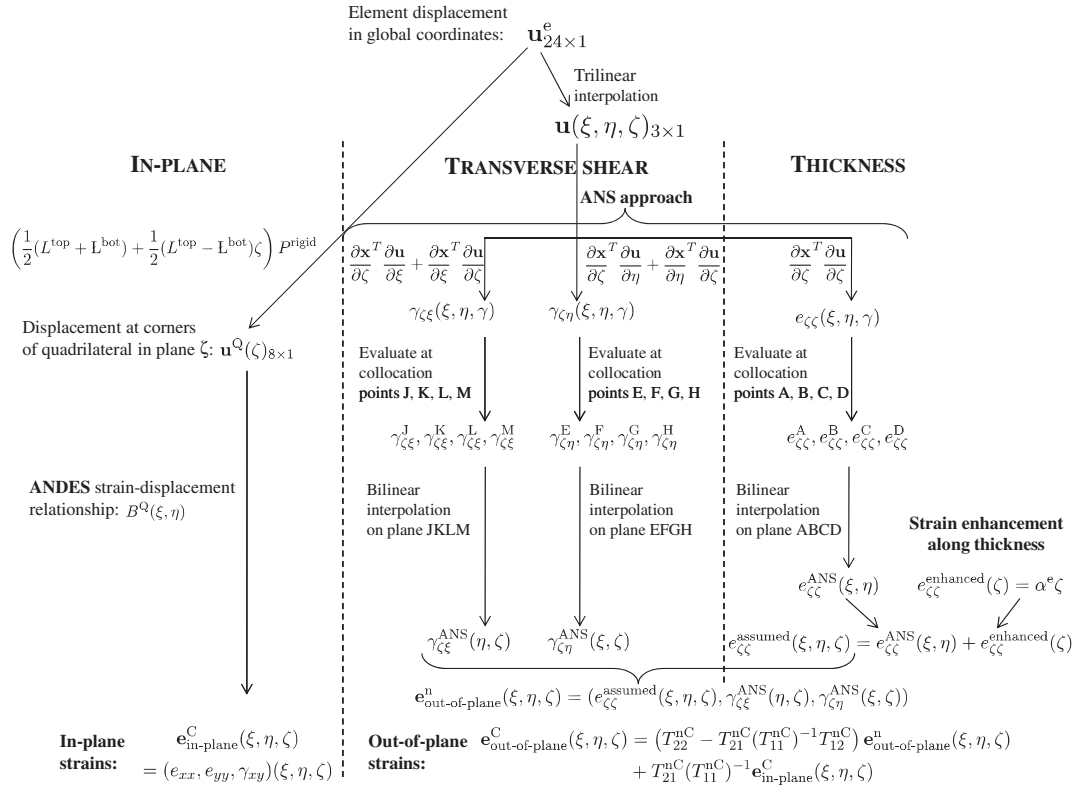


Figure 4. Derivation of assumed strain field.

the vector of strain components in natural coordinates. Both vectors, however, are expressed as functions of the natural coordinates to facilitate numerical integration using Gauss quadrature. Furthermore, the subscripts ‘in-plane’ and ‘out-of-plane’ are used to denote collections of the in-plane and out-of-plane parts of these strain vectors. The transformation of natural strain components to Cartesian strain components in local coordinates is given by

$$\mathbf{e}^C(\xi, \eta, \zeta) = T^{\text{nC}}(\xi, \eta, \zeta)\mathbf{e}^n(\xi, \eta, \zeta) \quad (14)$$

where

$$T^{\text{nC}} = \begin{bmatrix} j_{11}^2 & j_{21}^2 & j_{11}j_{21} & j_{31}^2 & j_{21}j_{31} & j_{11}j_{31} \\ j_{12}^2 & j_{22}^2 & j_{12}j_{22} & j_{32}^2 & j_{22}j_{32} & j_{12}j_{32} \\ 2j_{11}j_{12} & 2j_{21}j_{22} & j_{12}j_{21} + j_{11}j_{22} & 2j_{31}j_{32} & j_{22}j_{31} + j_{21}j_{32} & j_{12}j_{31} + j_{11}j_{32} \\ j_{13}^2 & j_{23}^2 & j_{13}j_{23} & j_{33}^2 & j_{23}j_{33} & j_{13}j_{33} \\ 2j_{12}j_{13} & 2j_{22}j_{23} & j_{13}j_{22} + j_{12}j_{23} & 2j_{32}j_{33} & j_{23}j_{32} + j_{22}j_{33} & j_{13}j_{32} + j_{12}j_{33} \\ 2j_{11}j_{13} & 2j_{21}j_{23} & j_{13}j_{21} + j_{11}j_{23} & 2j_{31}j_{33} & j_{23}j_{31} + j_{21}j_{33} & j_{13}j_{31} + j_{11}j_{33} \end{bmatrix} \quad (15)$$

with j_{pq} , $p, q = 1, \dots, 3$ being the components of the inverse of the jacobian matrix (11). This can also be written in a partitioned format as

$$\begin{pmatrix} \mathbf{e}_{\text{in-plane}}^C \\ \mathbf{e}_{\text{out-of-plane}}^C \end{pmatrix} = \begin{bmatrix} T_{11}^{\text{nC}} & T_{12}^{\text{nC}} \\ T_{21}^{\text{nC}} & T_{22}^{\text{nC}} \end{bmatrix} \begin{pmatrix} \mathbf{e}_{\text{in-plane}}^n \\ \mathbf{e}_{\text{out-of-plane}}^n \end{pmatrix} \quad (16)$$

3.2.1. In-plane strains. The in-plane strain field is constructed by applying the ANDES formulation of Section 2 to each quadrilateral cross-section of the solid-shell element in the thickness direction. When applied to warped elements, this is found to result in nonzero in-plane Cartesian strains for rigid body displacements of the element, that is, rigid body motions produce nonzero

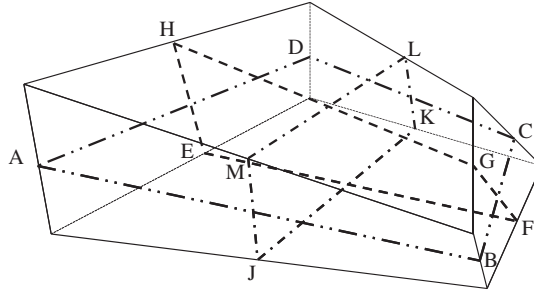


Figure 5. Collocation points of the Assumed Natural Strain approach.

in-plane strains. To avoid this problem, rigid body components are projected out of the displacement vector using a projection matrix P^{rigid} , before applying the strain-displacement operator. The approach is similar to that used by Rankin and coworkers [43, 60]. The x and y components of the displacement at the corners of a quadrilateral are then approximated by[§]

$$\mathbf{u}^Q(\zeta) = \frac{1}{2}(1 + \zeta)L^{\text{top}}P^{\text{rigid}}\mathbf{u}^e + \frac{1}{2}(1 - \zeta)L^{\text{bot}}P^{\text{rigid}}\mathbf{u}^e \quad (17)$$

with $P^{\text{rigid}} = \mathbf{I} - \mathbf{\Lambda}(\mathbf{\Lambda}^T\mathbf{\Lambda})^{-1}\mathbf{\Lambda}$.

Here, L^{top} and L^{bot} are Boolean matrices that extract the x and y displacement components of nodes (1, 2, 3, 4) and nodes (5, 6, 7, 8), respectively, whereas $\mathbf{\Lambda}$ contains the first six columns of the G_{rc} matrix introduced by Bergan in [37, 38].

Applying the strain-displacement operator from Equation (4) gives the in-plane strain field and the corresponding strain-displacement operator.

$$\begin{aligned} \mathbf{e}_{\text{in-plane}}^C(\xi, \eta, \zeta) &= B^Q(\xi, \eta)\mathbf{u}^Q(\zeta) \\ &= \underbrace{B^Q(\xi, \eta)\frac{1}{2}(L^{\text{top}} + L^{\text{bot}})P^{\text{rigid}}\mathbf{u}^e}_{\text{membrane}} + \underbrace{B^Q(\xi, \eta)\frac{1}{2}(L^{\text{top}} - L^{\text{bot}})\zeta P^{\text{rigid}}\mathbf{u}^e}_{\text{bending}} \quad (18) \\ &= B_{\text{in-plane}}^C(\xi, \eta, \zeta)\mathbf{u}^e \end{aligned}$$

It is seen that the in-plane strain field consists of membrane and out-of-plane bending components. The former is uniform across the thickness, whereas the latter varies linearly over it.

3.2.2. Transverse shear strains. Transverse shear strains are approximated using the ANS concept. Compatible natural strain components corresponding to transverse shear are obtained as

$$\begin{aligned} \gamma_{\xi\zeta}(\xi, \eta, \zeta) &= \left(\frac{\partial \mathbf{x}}{\partial \zeta}\right)^T \left(\frac{\partial \mathbf{u}}{\partial \xi}\right) + \left(\frac{\partial \mathbf{x}}{\partial \xi}\right)^T \left(\frac{\partial \mathbf{u}}{\partial \zeta}\right) \\ \gamma_{\eta\zeta}(\xi, \eta, \zeta) &= \left(\frac{\partial \mathbf{x}}{\partial \zeta}\right)^T \left(\frac{\partial \mathbf{u}}{\partial \eta}\right) + \left(\frac{\partial \mathbf{x}}{\partial \eta}\right)^T \left(\frac{\partial \mathbf{u}}{\partial \zeta}\right) \end{aligned} \quad (19)$$

[§] $\mathbf{u}^Q(\zeta)$ is an exception to the general vector notation used in this paper. It denotes the collection of x and y components of the displacements at the corners of the quadrilateral cross-section of constant natural coordinate ζ

Each of these strain components is evaluated at the four collocation points shown in Figure 5. The four values are bilinearly interpolated to obtain the assumed strain field, which may be expressed as

$$\begin{aligned}\gamma_{\eta\zeta}^{\text{ANS}} &= \sum_{i=E}^H N_{\gamma_{\eta\zeta}}^i(\xi, \zeta) \gamma_{\eta\zeta}(\xi^i, \zeta^i), \quad N_{\gamma_{\eta\zeta}}^i(\xi, \zeta) = \frac{1}{4}(1 + \xi^i \xi)(1 + \zeta^i \zeta), \quad i = E, \dots, H \\ \gamma_{\xi\zeta}^{\text{ANS}} &= \sum_{i=J}^M N_{\gamma_{\xi\zeta}}^i(\eta, \zeta) \gamma_{\xi\zeta}(\eta^i, \zeta^i), \quad N_{\gamma_{\xi\zeta}}^i(\eta, \zeta) = \frac{1}{4}(1 + \eta^i \eta)(1 + \zeta^i \zeta), \quad i = J, \dots, M\end{aligned}\quad (20)$$

Cardoso *et al.* [26] have shown that this approach is effective in alleviating transverse shear locking. In fully-integrated solid-shell elements, many authors have used only two collocation points per transverse shear term (for example, [19, 27, 30]). However, it is found that such an element is still susceptible to curvature locking in the presence of inextensional bending. Furthermore, in reduced-integration elements, the use of two collocation points leads to a rank deficient stiffness matrix [21, 26].

3.2.3. Thickness strain. The thickness strain field is constructed by a combination of the ANS and EAS approaches. These are discussed in order.

The ANS approach for the thickness strain field follows along the same lines as for transverse shear strains. First the natural strain component corresponding to the thickness direction is obtained from

$$\gamma_{\eta\zeta}(\xi, \eta, \zeta) = \left(\frac{\partial \mathbf{x}}{\partial \zeta} \right)^T \left(\frac{\partial \mathbf{u}}{\partial \zeta} \right) \quad (21)$$

This is evaluated at the collocation points (A, B, C, D) shown in Figure 5 and bilinearly interpolated:

$$e_{\zeta\zeta}^{\text{ANS}}(\xi, \eta) = \sum_{i=A}^D N_{e_{\zeta\zeta}}^i(\xi, \eta) \gamma_{\eta\zeta}(\xi^i, \eta^i), \quad N_{e_{\zeta\zeta}}^i(\xi, \eta) = \frac{1}{4}(1 + \xi^i \xi)(1 + \eta^i \eta), \quad i = A, \dots, D \quad (22)$$

It has been shown by Schwarze *et al.* [21], involving curved shells, that for thickness tapered elements, this assumed strain is a good remedy to alleviate thickness curvature locking. The numerical solutions presented in Section 5 corroborate those findings.

Cartesian strain components: It is recognized that Equation (18) gives Cartesian components of in-plane strains, whereas Equations (19) and (21) give natural components of out-of-plane strains. The Cartesian components of the out-of-plane strains are obtained using Equation (16) as follows

$$\begin{aligned}\mathbf{e}_{\text{out-of-plane}}^C(\xi, \eta, \zeta) &= \left(T_{22}^{\text{nC}} - T_{21}^{\text{nC}} (T_{11}^{\text{nC}})^{-1} T_{12}^{\text{nC}} \right) \mathbf{e}_{\text{out-of-plane}}^{\text{n}}(\xi, \eta, \zeta) \\ &\quad + T_{21}^{\text{nC}} (T_{11}^{\text{nC}})^{-1} \mathbf{e}_{\text{in-plane}}^C(\xi, \eta, \zeta)\end{aligned}\quad (23)$$

This in turn can be written as

$$\mathbf{e}_{\text{out-of-plane}}^C(\xi, \eta, \zeta) = B_{\text{out-of-plane}}^C(\xi, \eta, \zeta) \mathbf{u}^e \quad (24)$$

Thus, the strain-displacement matrix for the element is

$$(B^{\text{ANS}}(\xi, \eta, \zeta))^C = \left[\frac{B_{\text{in-plane}}^C(\xi, \eta, \zeta)}{B_{\text{out-of-plane}}^C(\xi, \eta, \zeta)} \right] \quad (25)$$

where $B(\xi, \eta, \zeta)^{\text{ANS}}$ is a 6×24 matrix.

Strain enhancement: The assumed natural thickness strain $e_{\xi\xi}^{ANS}$ is independent of ζ . This may cause thickness locking, particularly in thick elements. To alleviate locking, we note that Poisson's effect would cause the thickness strain associated with bending to vary linearly. By using the EAS concept, the assumed natural thickness strain is enhanced by a thickness-dependent component:

$$\left(e_{\xi\xi}^{\text{enhanced}}(\zeta)\right)^n = \alpha^e \zeta \quad (26)$$

in which α^e is a condensable EAS DOF. Thus, the total strain field for the element is given by

$$\begin{aligned} e_{\text{elem}}^C &= \begin{bmatrix} (B^{ANS}(\xi, \eta, \zeta))^C & (B^{\text{enhanced}}(\zeta))^C \end{bmatrix} \begin{pmatrix} \mathbf{u}^e \\ \alpha^e \end{pmatrix} = \mathbf{B}_{\text{elem}} \begin{pmatrix} \mathbf{u}^e \\ \alpha^e \end{pmatrix} \\ \text{with } (B^{\text{enhanced}}(\zeta))^C &= T_0^{nC} (B^{\text{enhanced}}(\zeta))^n \\ \text{and } (B^{\text{enhanced}}(\zeta))^n &= \begin{bmatrix} 0 & 0 & 0 & \zeta & 0 & 0 \end{bmatrix}^T \end{aligned} \quad (27)$$

Here, the last column of \mathbf{B}_{elem} , which is a 6×25 matrix, corresponds to the enhanced strain DOF in the thickness direction. T_0^{nC} is the transformation matrix (15) evaluated at $\xi = \eta = \zeta = 0$. It is noted that the enhanced strain is constant in the shell plane.

The element stiffness matrix in local coordinates, K_1 , is obtained by computing $\int_V \mathbf{B}_{\text{elem}}^T E \mathbf{B}_{\text{elem}} dV$ and eliminating the enhanced strain DOF by static condensation. This can be transformed to the representation of the stiffness matrix in global coordinates in the usual manner.

4. COROTATIONAL FORMULATION

4.1. Kinematic description

In this section, the solid-shell element formulation is extended to the geometric nonlinear regime using a CR kinematic description. This description is based on decomposing the motion of an element into rigid body and deformation components. Deformations are described with reference to a coordinate frame that translates and rotates with the element as shown in Figure 6. An attractive feature of the CR description, particularly for small strain problems, is that elements that perform well in geometrically linear problems can be extended to nonlinear problems in an *element-independent*

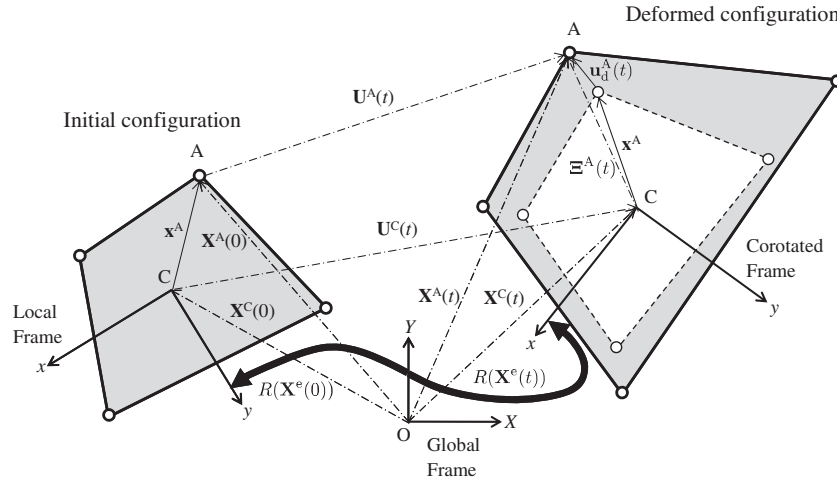


Figure 6. Corotational element kinematics highlighting the motion of a point A. For clarity, a two-dimensional setting is shown the figure. \mathbf{X}^C is the average of the positions of the element nodes. Vectors represented by components in a local frame (\mathbf{x}^A and \mathbf{u}_d^A) are shown in solid arrows, and those represented by components in the global frame by dash-dot arrows. It can be seen that $\Xi^A(t) = \mathbf{X}^A(t) - \mathbf{X}^C(t) = R(\mathbf{X}^e(t)) (\mathbf{x}^A + \mathbf{u}_d^A(t))$.

fashion. This approach, referred to as an EICR, was introduced by Rankin and Brogan [59]. Felippa and Haugen [52, 58] presented a unified formulation of the CR approach for 3D elements with both translational and rotational DOF. In this paper, this unified formulation is adopted, and proofs of some results are presented in greater detail.

For a given deformed configuration, that is, node positions with respect to the global frame, there are a number of strategies for constructing a corotated reference frame. In the formulation presented here, the origin of the corotated frame, C , is established by simply averaging the positions of the element nodes. The orientation R of the corotated frame depends on the positions of the nodes \mathbf{X}^e . The specific construction of $R(\mathbf{X}^e)$ used in this work is described in Section 4.2. In the remainder of this section, some generic relationships are derived assuming only the following invariance properties of $R(\mathbf{X}^e)$.

1. *Rotation invariance:* If all the nodes are subject to a rigid body rotation Q , then the resulting corotated frame is also rotated by Q .

$$R(\text{diag}(Q)\mathbf{X}^e) = QR(\mathbf{X}^e) \text{ for any rotation matrix } Q \quad (28)$$

2. *Translation invariance:* A uniform translation of all the nodes by \mathbf{v} does not alter the orientation of the corotated frame.

$$R(\mathbf{X}^e + \text{stack}(\mathbf{v})) = R(\mathbf{X}^e) \text{ for any 3-vector } \mathbf{v} \quad (29)$$

where diag and stack are as defined in (6).

From Figure 6, it can be deduced that for node A,

$$R(\mathbf{X}^e(t))(\mathbf{x}^A + \mathbf{u}_d^A(t)) = \mathbf{X}^A(t) - \mathbf{X}^C(t) \quad (30)$$

or rewriting,

$$\mathbf{u}_d^A(t) = R(\mathbf{X}^e(t))^T(\mathbf{X}^A(t) - \mathbf{X}^C(t)) - R(\mathbf{X}^e(0))^T(\mathbf{X}^A(0) - \mathbf{X}^C(0)) \quad (31)$$

These expressions can be collected for all the nodes of the element, thus providing the element deformational displacement as

$$\mathbf{u}_d^e(t) = \mathcal{R}(\mathbf{X}^e(t))^T(\mathbf{X}^e(t) - \text{stack}(\mathbf{X}^C(t))) - \mathcal{R}(\mathbf{X}^e(0))^T(\mathbf{X}^e(0) - \text{stack}(\mathbf{X}^C(0))) \quad (32)$$

where $\mathcal{R} = \text{diag}(R)$. Further, by defining $P_T = \frac{1}{n} \text{array}(I_{3 \times 3})$, $\text{stack}(\mathbf{X}^C)$ can be written as $\text{stack}(\mathbf{X}^C) = P_T \mathbf{X}^e$; by defining $\Xi^e = (I - P_T)\mathbf{X}^e$ and using the translation invariance property (29) of R , Equation (32) becomes

$$\mathbf{u}_d^e(t) = \mathcal{R}(\Xi^e(t))^T \Xi^e(t) - \mathcal{R}(\Xi^e(0))^T \Xi^e(0) \quad (33)$$

To obtain a relationship between change in displacement and change in deformational displacement, Equation (33) is differentiated with respect to time.

$$\dot{\mathbf{u}}_d^e = \mathcal{R}(\Xi^e(t))^T \dot{\Xi}^e + (D\mathcal{R}(\Xi^e(t))\dot{\Xi}^e)^T \Xi^e(t) \quad (34)$$

where D denotes the derivative. It follows from the fact that $R(\Xi^e(t))R(\Xi^e(t))^T = I$ for all t , that $(D\mathcal{R}(\Xi^e(t))\dot{\Xi}^e)R(\Xi^e(t))^T$ is a skew-symmetric matrix. Furthermore, $(D\mathcal{R}(\Xi^e(t))\dot{\Xi}^e)R(\Xi^e(t))^T$ is linear in $\dot{\Xi}^e$. Consequently, this term can be written as

$$(D\mathcal{R}(\Xi^e(t))\dot{\Xi}^e)R(\Xi^e(t))^T = \text{spin}(G(\Xi^e(t))\dot{\Xi}^e) \quad (35)$$

where

$$\text{spin}(\mathbf{v}) = \begin{bmatrix} 0 & -v_3 & v_2 \\ v_3 & 0 & -v_1 \\ -v_2 & v_1 & 0 \end{bmatrix} \quad (36)$$

It is also noted that $\text{spin}(\mathbf{v})\mathbf{u} = \mathbf{v} \times \mathbf{u}$. The matrix $G(\mathbf{\Xi}^e)$ can be interpreted as the operation of extracting the spatial angular velocity from an instantaneous motion starting from the configuration $\mathbf{\Xi}^e$.

By using (35), Equation (34) can be written as

$$\dot{\mathbf{u}}_d^e = \mathcal{R}(\mathbf{\Xi}^e(t))^T \dot{\mathbf{\Xi}}^e - \mathcal{R}(\mathbf{\Xi}^e(t))^T \text{diag} \left(\text{spin} \left(G(\mathbf{\Xi}^e(t)) \dot{\mathbf{\Xi}}^e \right) \right) \mathbf{\Xi}^e(t) \quad (37)$$

Moreover, corresponding to each node n ,

$$\begin{aligned} \text{spin} \left(G(\mathbf{\Xi}^e(t)) \dot{\mathbf{\Xi}}^e \right) \mathbf{\Xi}^n(t) &= \left(G(\mathbf{\Xi}^e(t)) \dot{\mathbf{\Xi}}^e \right) \times \mathbf{\Xi}^n(t) \\ &= -\mathbf{\Xi}^n(t) \times \left(G(\mathbf{\Xi}^e(t)) \dot{\mathbf{\Xi}}^e \right) = -\text{spin}(\mathbf{\Xi}^n(t)) G(\mathbf{\Xi}^e(t)) \dot{\mathbf{\Xi}}^e \end{aligned} \quad (38)$$

Therefore, by setting

$$S(\mathbf{\Xi}^e) = \left[-\text{spin}(\mathbf{\Xi}^1)^T, -\text{spin}(\mathbf{\Xi}^2)^T, \dots, -\text{spin}(\mathbf{\Xi}^n)^T \right]^T \quad (39)$$

and

$$P_R(\mathbf{\Xi}^e) = S(\mathbf{\Xi}^e) G(\mathbf{\Xi}^e) \quad (40)$$

and using the fact that $\dot{\mathbf{\Xi}}^e = (I - P_T) \dot{\mathbf{U}}^e$, Equation (37) can be written as

$$\dot{\mathbf{u}}_d^e = \mathcal{R}(\mathbf{\Xi}^e(t))^T (I - P_R(\mathbf{\Xi}^e(t))) (I - P_T) \dot{\mathbf{U}}^e \quad (41)$$

In the following, some results concerning the matrices P_T and $P_R(\mathbf{\Xi}^e)$ are derived.

- (i) P_T is a projector: By direct calculation, it can be verified that $P_T^2 = P_T$.
- (ii) $P_R(\mathbf{\Xi}^e)$ is a projector: $P_R(\mathbf{\Xi}^e)^2 = S(\mathbf{\Xi}^e) G(\mathbf{\Xi}^e) S(\mathbf{\Xi}^e) G(\mathbf{\Xi}^e)$. To show that $P_R(\mathbf{\Xi}^e)$ is a projector, it is sufficient to show that $G(\mathbf{\Xi}^e) S(\mathbf{\Xi}^e) = I$, or equivalently that $G(\mathbf{\Xi}^e) S(\mathbf{\Xi}^e) \boldsymbol{\omega} = \boldsymbol{\omega}$ for any $\boldsymbol{\omega}$.

$S(\mathbf{\Xi}^e) \boldsymbol{\omega} = \text{diag}(\text{spin}(\boldsymbol{\omega})) \mathbf{\Xi}^e$. Therefore, $S(\mathbf{\Xi}^e) \boldsymbol{\omega}$ is the velocity of the nodes when the element is subject to a rigid body rotation with spatial angular velocity $\boldsymbol{\omega}$. From the interpretation of $G(\mathbf{\Xi}^e)$ as the operation of extracting the angular velocity, it can be conjectured that $G(\mathbf{\Xi}^e) S(\mathbf{\Xi}^e) \boldsymbol{\omega} = \boldsymbol{\omega}$. However, a formal proof is as follows.

Let $\tilde{\mathbf{\Xi}}^e(\tau)$ represent the position relative to \mathbf{X}^C at time τ of the n^e nodes of the element, starting at $\tilde{\mathbf{\Xi}}^e(0) = \mathbf{\Xi}^e$ and undergoing rigid body rotation about \mathbf{X}^C with constant angular velocity $\boldsymbol{\omega}$. The motion is described by the differential equation

$$\dot{\tilde{\mathbf{\Xi}}}^e(\tau) = \text{diag}(\text{spin}(\boldsymbol{\omega})) \tilde{\mathbf{\Xi}}^e(\tau) \quad (42)$$

The solution of this differential equation is $\tilde{\mathbf{\Xi}}^e(\tau) = \text{diag}(\bar{Q}(\tau)) \tilde{\mathbf{\Xi}}^e(0)$ where $\bar{Q}(\tau)$ is a rotation matrix given by $\bar{Q}(\tau) = \exp(\text{spin}(\boldsymbol{\omega})\tau)$, \exp being the matrix exponential. \bar{Q} satisfies $\dot{\bar{Q}}(\tau) \bar{Q}(\tau)^T = \text{spin}(\boldsymbol{\omega})$ for all τ . Then

$$\begin{aligned}
& \text{spin} \left(G \left(\tilde{\Xi}^e(\tau) \right) S \left(\tilde{\Xi}^e(\tau) \right) \omega \right) \\
&= \left(D \hat{R} \left(\tilde{\Xi}^e(\tau) \right) S \left(\tilde{\Xi}^e(\tau) \right) \omega \right) \hat{R} \left(\tilde{\Xi}^e(\tau) \right) \text{ by the definition of } G, \text{ Equation (35)} \\
&= \left(D \hat{R} \left(\tilde{\Xi}^e(\tau) \right) \text{diag}(\text{spin}(\omega)) \tilde{\Xi}^e(\tau) \right) \hat{R} \left(\tilde{\Xi}^e(\tau) \right) \\
&= \left(D \hat{R} \left(\tilde{\Xi}^e(\tau) \right) \dot{\tilde{\Xi}}^e \right) \hat{R}(\tilde{\Xi}^e(\tau)) \text{ by Equation (42)} \\
&= \left(\frac{d}{dt} \hat{R} \left(\tilde{\Xi}^e(\tau) \right) \right) \hat{R} \left(\tilde{\Xi}^e(\tau) \right)^T \\
&= \left(\frac{d}{dt} \hat{R}(\text{diag}(\bar{Q}(\tau)) \tilde{\Xi}^e(0)) \right) \hat{R} \left(\text{diag}(\bar{Q}(\tau)) \tilde{\Xi}^e(0) \right)^T \\
&= \left(\frac{d}{dt} \bar{Q}(\tau) \hat{R} \left(\tilde{\Xi}^e(0) \right) \right) \left(\bar{Q}(\tau) \hat{R} \left(\tilde{\Xi}^e(0) \right) \right)^T \text{ by the rotation invariance property (28)} \\
&= \dot{\bar{Q}}(\tau) \hat{R} \left(\tilde{\Xi}^e(0) \right) \hat{R} \left(\tilde{\Xi}^e(0) \right)^T \bar{Q}(\tau)^T \\
&= \dot{\bar{Q}}(\tau) \bar{Q}(\tau)^T \\
&= \text{spin}(\omega)
\end{aligned}$$

Thus, $G \left(\tilde{\Xi}^e(\tau) \right) S \left(\tilde{\Xi}^e(\tau) \right) \omega = \omega$ for all τ , in particular for $\tau = 0$. Hence, $G(\Xi^e)S(\Xi^e)\omega = \omega$, and $P_R(\Xi^e)$ is a projector.

- (iii) *The product $P_T P_R(\Xi^e) = 0$:* It can be verified by direct calculation that $P_T S(\Xi^e) = 0$. Thus, $P_T P_R(\Xi^e) = P_T S(\Xi^e) G(\Xi^e) = 0$.
- (iv) *The product $P_R(\Xi^e) P_T = 0$:* Each column of P_T is of the form $\text{stack}(\mathbf{v})$ for $\mathbf{v} = (1, 0, 0)^T, (0, 1, 0)^T, (0, 0, 1)^T$. Therefore, to show that $P_R(\Xi^e) P_T = 0$, it is sufficient to show that $G(\Xi^e) \text{stack}(\mathbf{v}) = 0$ for any \mathbf{v} .

$\text{stack}(\mathbf{v})$ is the velocity of the nodes when the element is subject to a uniform rigid body motion with velocity \mathbf{v} . Again from the interpretation of $G(\Xi^e)$ as extracting the angular velocity, it can be supposed that $G(\Xi^e) \text{stack}(\mathbf{v}) = 0$. The following is the complete proof.

Let $\tilde{\Xi}^e(\tau)$ represent the position relative to \mathbf{X}^C at time τ of the n^e nodes of the element, starting at $\tilde{\Xi}^e(0) = \Xi^e$ and undergoing rigid body motion with constant velocity \mathbf{v} . Then $\tilde{\Xi}^e(\tau) = \Xi^e + \text{stack}(\mathbf{v})\tau$.

$$\begin{aligned}
& G \left(\tilde{\Xi}^e(t) \right) \text{stack}(\mathbf{v}) \\
&= \left(D \hat{R} \left(\tilde{\Xi}^e(t) \right) \text{stack}(\mathbf{v}) \right) \hat{R} \left(\tilde{\Xi}^e(t) \right) \text{ by the definition of } G, \text{ Equation (35)} \\
&= \left(D \hat{R} \left(\tilde{\Xi}^e(t) \right) \dot{\tilde{\Xi}}^e \right) \hat{R} \left(\tilde{\Xi}^e(t) \right) \\
&= \left(\frac{d}{dt} \hat{R} \left(\tilde{\Xi}^e(t) \right) \right) \hat{R} \left(\tilde{\Xi}^e(t) \right)^T \\
&= \left(\frac{d}{dt} \hat{R}(\Xi^e) \right) \hat{R}(\Xi^e)^T \text{ by the translation invariance property (29)} \\
&= 0.
\end{aligned}$$

By using property (iv), Equation (41) can be written as

$$\dot{\mathbf{u}}_d^e = \mathcal{R}(\Xi^e(t))^T (I - P_T - P_R(\Xi^e(t))) \dot{\mathbf{U}}^e \quad (43)$$

or defining $\mathcal{P}(\Xi^e) = I - P_T - P_R(\Xi^e)$ as

$$\dot{\mathbf{u}}_d^e = \mathcal{R}(\Xi^e(t))^T \mathcal{P}(\Xi^e(t)) \dot{\mathbf{U}}^e \quad (44)$$

Furthermore, it can be checked using properties (i)–(iv) that $\mathcal{P}(\Xi^e)^2 = \mathcal{P}(\Xi^e)$, that is, $\mathcal{P}(\Xi^e)$ is a projector. It can be seen in Equation (44) that the corotated deformational velocity $\dot{\mathbf{u}}_d^e$ is obtained from the global velocity vector $\dot{\mathbf{U}}^e$ by a project-and-rotate operation, first a projection $\mathcal{P}(\Xi^e)$, and then a rotation $\mathcal{R}(\Xi^e)^T$. Alternatively, a rotate-and-project approach is also possible [52]. Next, the specific strategy used in this paper to construct the corotated frame orientation, $R(\Xi^e)$, is described.

4.2. Construction of the corotated frame

Different methods have been proposed in the literature for constructing the corotated frame R for quadrilateral shell elements; see for example [41, 52, 59]. Fraeijs de Veubeke defined the orientation (over a complete structure, such as an aircraft) by minimizing the mean square of relative displacements [69]. Belytschko and Bindeman [70] and Moita and Crisfield [57] derived from the polar decomposition of the deformation gradient tensor evaluated at the element center. This approach was also followed by Abed-Meriam and Combescure for a solid-shell element [46].

In the present work, the corotated frame is constructed in the same manner as the local frame in Section 3.1.1. However, current node coordinates $\Xi^e(t)$ are used in Equation (7). The partial derivatives $\frac{\partial}{\partial \Xi_j^e} R(\Xi^e)$ can be obtained from Equation (7) by noting that

$$D||\mathbf{v}|| = \frac{1}{||\mathbf{v}||} \mathbf{v}^T \quad (45)$$

for $\mathbf{v} \neq 0$ and using the chain rule. From Equation (35), it follows that the j th column of the matrix $G(\Xi^e)$ is given by

$$\text{axial} \left(\left(\frac{\partial}{\partial \Xi_j^e} R(\Xi^e) \right) R(\Xi^e)^T \right) \quad (46)$$

where axial is the vector representation of a 3×3 skew-symmetric matrix, that is, the inverse of the spin operation defined in Equation (36).

4.3. Tangent stiffness matrix

The internal force vector with components referred to the global and local coordinate systems, respectively, is given by

$$\begin{aligned} \mathbf{f}^e &= K_I \mathbf{u}_d^e \\ \mathbf{F}^e &= \mathcal{P}(\Xi^e)^T \mathcal{R}(\Xi^e) \mathbf{f}^e \end{aligned} \quad (47)$$

The tangent stiffness matrix needed for Newton's method can be obtained by considering the rate of change of the internal force vector.

$$\begin{aligned} \dot{\mathbf{F}}^e &= \mathcal{P}(\Xi^e)^T \mathcal{R}(\Xi^e) \dot{\mathbf{f}}^e \\ &+ (I - P_T)^T \frac{d}{dt} \mathcal{R}(\Xi^e) \mathbf{f}^e - G(\Xi^e)^T \frac{d}{dt} S(\Xi^e)^T \mathcal{R}(\Xi^e) \mathbf{f}^e \\ &- G(\Xi^e)^T S(\Xi^e)^T \frac{d}{dt} \mathcal{R}(\Xi^e) \mathbf{f}^e \\ &- \frac{d}{dt} G(\Xi^e)^T S(\Xi^e)^T \mathcal{R}(\Xi^e) \mathbf{f}^e \end{aligned} \quad (48)$$

Each of these terms is considered in turn. The first term,

$$\mathcal{P}(\Xi^e)^T \mathcal{R}(\Xi^e) \dot{\mathbf{f}}^e = \mathcal{P}(\Xi^e)^T \mathcal{R}(\Xi^e) K_I \dot{\mathbf{u}}_d^e = \mathcal{P}(\Xi^e)^T \mathcal{R}(\Xi^e) K_I \dot{\mathbf{u}}_d^e \mathcal{R}(\Xi^e)^T \mathcal{P}(\Xi^e) \dot{\mathbf{U}}^e = K_M \dot{\mathbf{U}}^e \quad (49)$$

gives rise to the ‘material’ stiffness matrix K_M . The second and third terms combine as follows.

$$\begin{aligned}
& (I - P_T)^T \frac{d}{dt} \mathcal{R}(\Xi^e) \mathbf{f}^e - G(\Xi^e)^T \frac{d}{dt} S(\Xi^e)^T \mathcal{R}(\Xi^e) \mathbf{f}^e \\
&= (I - P_T)^T \left(D \mathcal{R}(\Xi^e) \dot{\Xi}^e \right) \mathcal{R}(\Xi^e)^T \mathcal{R}(\Xi^e) \mathbf{f}^e - G(\Xi^e)^T S \left(\dot{\Xi}^e \right)^T \mathcal{R}(\Xi^e) \mathbf{f}^e \\
&= (I - P_T)^T \text{diag} \left(\text{spin} \left(G(\Xi^e) \dot{\Xi}^e \right) \right) \mathcal{R}(\Xi^e) \mathbf{f}^e - G(\Xi^e)^T S \left(\dot{\Xi}^e \right)^T \mathcal{R}(\Xi^e) \mathbf{f}^e \\
&= (I - P_T)^T S(\mathcal{R}(\Xi^e) \mathbf{f}^e) G(\Xi^e) \dot{\Xi}^e + G(\Xi^e)^T S(\mathcal{R}(\Xi^e) \mathbf{f}^e)^T \dot{\Xi}^e \\
&= (I - P_T)^T S(\mathcal{R}(\Xi^e) \mathbf{f}^e) G(\Xi^e) (I - P_T) \dot{\mathbf{U}}^e + G(\Xi^e)^T S(\mathcal{R}(\Xi^e) \mathbf{f}^e)^T (I - P_T) \dot{\mathbf{U}}^e \\
&= \left(S(\mathcal{R}(\Xi^e) \mathbf{f}^e) G(\Xi^e) + (S(\mathcal{R}(\Xi^e) \mathbf{f}^e) G(\Xi^e))^T \right) \dot{\mathbf{U}}^e \quad (\text{from results (iii) and (iv) previously}) \\
&= K_G^I \dot{\mathbf{U}}^e
\end{aligned} \tag{50}$$

K_G^I , which is clearly symmetric, is one component of the geometric stiffness matrix. For the last two terms of (48), the arguments of Nour-Omid and Rankin [60] are used. For any three-vectors \mathbf{u} and \mathbf{v} , and rotation matrix R , it can be verified by direct calculation that

$$\begin{aligned}
\text{spin}(R\mathbf{u}) &= R \text{spin}(\mathbf{u}) R^T \\
\mathbf{u} \times (R\mathbf{v}) &= R \left((R^T \mathbf{u}) \times \mathbf{v} \right)
\end{aligned} \tag{51}$$

$$\text{spin}(\mathbf{u}) \text{spin}(\mathbf{v}) - \text{spin}(\mathbf{v}) \text{spin}(\mathbf{u}) = \text{spin}(\mathbf{u} \times \mathbf{v})$$

Rotational equilibrium of an element (expressed in local coordinates) requires

$$\begin{aligned}
0 &= \sum_{n=1}^{n^e} (R(\Xi^e(0))^T \Xi^n(0)) \times \mathbf{f}^n \\
&= R(\Xi^e)^T \sum_{n=1}^{n^e} (R(\Xi^e) R(\Xi^e(0))^T \Xi^n(0)) \times (R(\Xi^e) \mathbf{f}^n) \\
&= -R(\Xi^e)^T S(\mathcal{R}(\Xi^e) \mathcal{R}(\Xi^e(0))^T \Xi^e(0))^T \mathcal{R}(\Xi^e) \mathbf{f}^e
\end{aligned} \tag{52}$$

whence, $S(\mathcal{R}(\Xi^e) \mathcal{R}(\Xi^e(0))^T \Xi^e(0))^T \mathcal{R}(\Xi^e) \mathbf{f}^e = 0$. Now, considering the fourth term of (48),

$$\begin{aligned}
& -G(\Xi^e)^T S(\Xi^e)^T \frac{d}{dt} \mathcal{R}(\Xi^e) \mathbf{f}^e \\
&= -G(\Xi^e)^T S(\Xi^e)^T \left(D \mathcal{R}(\Xi^e) \dot{\Xi}^e \right) \mathcal{R}(\Xi^e)^T \mathcal{R}(\Xi^e) \mathbf{f}^e \\
&= -G(\Xi^e)^T S(\Xi^e)^T \text{diag} \left(\text{spin}(G(\Xi^e) \dot{\Xi}^e) \right) \mathcal{R}(\Xi^e) \mathbf{f}^e \\
&= -G(\Xi^e)^T S(\Xi^e)^T S(\mathcal{R}(\Xi^e) \mathbf{f}^e) G(\Xi^e) \dot{\Xi}^e \\
&= -G(\Xi^e)^T S(\Xi^e)^T S(\mathcal{R}(\Xi^e) \mathbf{f}^e) G(\Xi^e) \dot{\mathbf{U}}^e
\end{aligned} \tag{53}$$

We now consider the anti-symmetric part of this matrix.

$$\begin{aligned}
& S(\Xi^e)^T S(\mathcal{R}(\Xi^e)\mathbf{f}^e) - S(\mathcal{R}(\Xi^e)\mathbf{f}^e)^T S(\Xi^e) \\
&= \sum_{n=1}^{n^e} \text{spin}(R(\Xi^e)\mathbf{f}^n) \text{spin}(\Xi^n) - \text{spin}(\Xi^n) \text{spin}(R(\Xi^e)\mathbf{f}^n) \\
&= \sum_{n=1}^{n^e} \text{spin}((R(\Xi^e)\mathbf{f}^n) \times \Xi^n) \\
&= - \sum_{n=1}^{n^e} \text{spin}(R(\Xi^e)((R(\Xi^e)^T \Xi^n) \times \mathbf{f}^n)) \\
&= -R(\Xi^e) \left(\sum_{n=1}^{n^e} (R(\Xi^e)^T \Xi^n) \times \mathbf{f}^n \right) R(\Xi^e)^T
\end{aligned} \tag{54}$$

If the deformational displacements are small, that is, $\|\Xi^e - \mathcal{R}(\Xi^e)\mathcal{R}(\Xi^e(0))^T \Xi^e(0)\|$ is small, then from the moment equilibrium equation previously, $S(\Xi^e)^T \mathcal{R}(\Xi^e)\mathbf{f}^e \approx 0$. Therefore, the anti-symmetric term previously can be neglected as is carried out in [57]. Thus,

$$K_G^{\text{II}} = -G(\Xi^e)^T \text{sym}(S(\Xi^e)^T S(\mathcal{R}(\Xi^e)\mathbf{f}^e)) G(\Xi^e) \tag{55}$$

where the sym operator produces the symmetric part of a matrix. In a similar manner, the fifth term in (48) can also be neglected. The approximate tangent stiffness matrix given by $K = K_M + K_G^{\text{I}} + K_G^{\text{II}}$ results in good convergence characteristics as demonstrated in the numerical examples.

5. NUMERICAL EXAMPLES

In this section, numerical benchmarks are analyzed to investigate the performance of the proposed solid-shell element in both geometrically linear and nonlinear cases. Results are compared with other formulations in the literature. For brevity in subsequent discussion, abbreviations similar to those used in [21] are used for these reference formulations as summarized in Table I.

5.1. Linear benchmark problems

5.1.1. Patch tests. The patch test is a standard approach for assessing the correctness of an element formulation [82, 83]. It also provides a valuable code verification tool. A model is subject to nodal displacements that analytically correspond to a state of constant strain. If the finite element model results in the same strain state as the analytical solution, the element under consideration is said to have passed the patch test. The patch test assesses the consistency of a finite element formulation [84]. It is particularly useful in evaluating elements developed using a mixture of techniques that render applying a rigorous convergence theory difficult or impractical [85].

MacNeal and Harder [86] proposed a set of membrane and bending patch tests for 3D finite elements such as solid elements and shell elements. The membrane patch test is more significant because it assesses the completeness and convergence of the element assemblage. But in the context of the shell and solid-shell elements, the bending patch test is also of great importance to evaluate the bending behavior of the formulation with only one element across the thickness. This issue is directly related to the need for mesh refinement across the thickness and the consequent computational costs. Following MacNeal and Harder [86], a plate of length $L = 0.24$ mm, width $B = 0.12$ mm and thickness $t = 0.001$ mm shown in Figure 7 is discretized using five distorted elements. The material behavior is modeled as isotropic linear elastic with modulus of elasticity, $E = 10^6$ N/mm² and Poisson's ratio, $\nu = 0.25$.

Table I. References used to compare solutions in numerical examples.

Abbreviation	Reference	Description
Full-integration solid and solid-shell elements		
Kli06	Klinkel <i>et al.</i> [31]	Mixed ANS solid shell (HSEE).
Kim05	Kim <i>et al.</i> [28]	ANS solid shell with plane stress assumption for thickness strains (XSolid85).
Alv03	Alves de Sousa <i>et al.</i> [22]	Eight-node EAS solid shell with twelve enhanced variables (HCis12).
Are03	Areias <i>et al.</i> [24]	EAS solid element with penalty stabilization.
Sze00	Sze <i>et al.</i> [29]	Hybrid stress ANS solid shell (ANS _{$\gamma\epsilon$} and ANS _{$\gamma\epsilon$} -HS).
Kas00	Kasper <i>et al.</i> [71]	Mixed enhanced strain element with nine enhanced variables (H1/ME9).
Reduced-integration solid and solid-shell elements		
Schw09	Schwarze and Reese [21, 44]	ANS/EAS solid shell with one EAS variable and using the Taylor expansion of the inverse Jacobian with respect to the element center (Q1ST).
Abed09	Abed-Meriam and Combescure [46]	Assumed strain solid shell with physical stabilization (SHB8PS).
Car08	Cardoso <i>et al.</i> [26]	ANS/EAS solid shell with one EAS variable (MRESS).
Ree07	Reese [72]	EAS solid shell (Q1SPs).
Alv05	Alves de Sousa <i>et al.</i> [73]	EAS/SRI solid shell with one EAS variable and SRI technique for transverse shear locking (RESS).
SC8R	ABAQUS continuum solid [74]	Reduced-integration continuum solid element of ABAQUS.
Full- and reduced-integration conventional shell elements		
CYSE	Cardoso <i>et al.</i> [75]	One-point quadrature shell element with stabilization of spurious energy modes.
Gru05	Gruttmann and Wagner [76]	ANS mixed stress element with reduced integration.
iCYSE-E4	Cardoso <i>et al.</i> [77]	Four-node reduced-integration shell element with four enhancing variables for membrane strains.
Car02	Cardoso <i>et al.</i> [78]	ANS element with reduced integration.
ANS _{γ} -EAS	Bischoff and Ramm [79]	Full-integration EAS shell, which takes the thickness stretch into account.
ANDES3	Militello and Felippa [36]	Full-integration triangular shell element with drilling degrees of freedom based on ANDES approach.
ANDES4	Haugen and Felippa [52]	Full-integration quadrilateral shell element with drilling degrees of freedom based on ANDES approach.
Parisch91	Parisch [80]	Full-integration ANS element.
Simo89	Simo and Fox [9]	Full-integration mixed ANS Stress element.
Stander89	Stander <i>et al.</i> [81]	Full-integration quadrilateral ANS element.
Bat85	Bathe and Dvorkin [7]	Full-integration quadrilateral ANS element.
S4R	ABAQUS shell element [74]	Four-node reduced-integration shell element with hourglass stabilization.

ANS, Assumed Natural Strain; EAS, Enhanced Assumed Strain.

Membrane patch test: In this first patch test, displacements of the exterior nodes are prescribed by the linear functions

$$U_X = 10^{-3} \left(X + \frac{Y}{2} \right), \quad U_Y = 10^{-3} \left(Y + \frac{X}{2} \right) \quad (56)$$

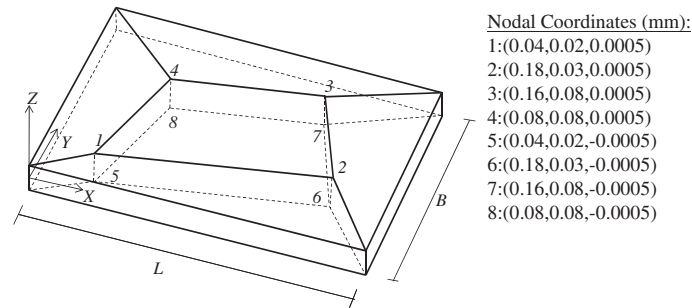


Figure 7. Patch test geometry.

with $U_Z = 0$ prescribed at the bottom layer of nodes, leading to a state of constant in-plane strain. Computed displacements of the interior nodes are shown in Table II. These agree exactly with the solution of Equation (56). The computed stresses at Gauss points are

$$\sigma_{XX} = \sigma_{YY} = 1333.33 \text{ N/mm}^2, \sigma_{XY} = 400.0 \text{ N/mm}^2 \quad (57)$$

with all other stress components being zero. These also agree with the analytical solution. The formulation thus passes the membrane patch test.

Bending patch test: In this test, the element patch shown in Figure 7 is tested to reproduce a constant curvature state. The displacements of exterior nodes are prescribed as

$$U_X = \mp t \frac{10^{-3}}{2} \left(X + \frac{Y}{2} \right), U_Y = \mp t \frac{10^{-3}}{2} \left(Y + \frac{X}{2} \right), U_Z = \frac{10^{-3}}{2} (X^2 + XY + Y^2) \quad (58)$$

resulting in constant curvature and implying a linear strain variation across the thickness. Computed displacements of the interior nodes are shown in Table III.

The stress components obtained at the top and bottom surfaces by extrapolating values computed at the Gauss points are

$$\sigma_{XX} = \sigma_{YY} = \pm 0.6667 \text{ N/mm}^2, \sigma_{XY} = \pm 0.200 \text{ N/mm}^2 \quad (59)$$

Both the computed displacements and stress components are identical to those from the analytical solution. Hence, the formulation also passes the bending patch test. The patch tests demonstrate that the ANDES approach performs well in accounting for the membrane response of the solid shell.

Table II. Membrane patch test – finite element solution.

Node	U_X (mm)	U_Y (mm)
1	5.000e-5	4.000e-5
2	1.950e-4	1.200e-4
3	2.000e-4	1.600e-4
4	1.200e-4	1.200e-4

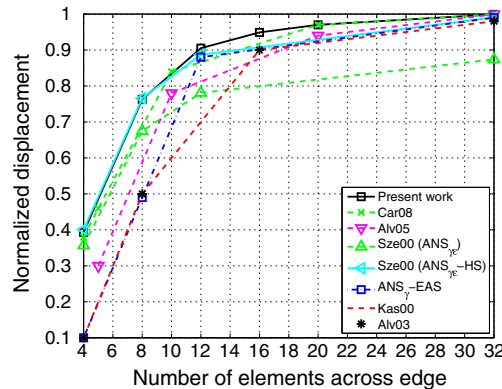
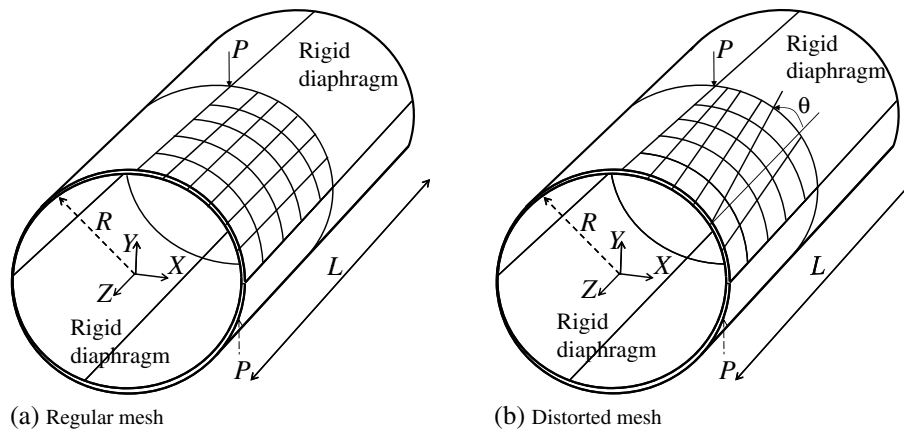
Table III. Bending patch test – finite element solution.

Node	U_X (mm)	U_Y (mm)	U_Z (mm)
1	-2.500e-8	-2.000e-8	1.400e-6
2	-9.750e-8	-6.000e-8	1.935e-5
3	-1.000e-7	-8.000e-8	2.240e-5
4	-6.000e-8	-6.000e-8	9.600e-6

5.1.2. Pinched cylinder with end diaphragms. This test is one of the three ‘obstacle course’ problems proposed by Belytschko for shell elements [87]. It assesses the performance of the element for inextensional bending and complex membrane modes. This is a challenging test for the solid-shell formulation because it involves both membrane and bending responses of the element. Another feature of this test is that the solid-shell formulation is checked for trapezoidal locking that could occur when modeling curved shells. Two mesh types are investigated – a regular mesh and a distorted mesh. The distorted mesh also causes the mid-surface to be warped. The cylinder model shown in Figure 8 is pinched by two diametrically opposite point loads of magnitude $P = 1.0$ N. The material behavior is modeled as isotropic linear elastic with $E = 3 \times 10^6$ N/mm² and $\nu = 0.3$. The radius, length and thickness of the cylinder are, respectively, $R = 300$ mm, $L = 600$ mm and $t = 3.0$ mm. Because of symmetry, only an eighth of the cylinder is represented with appropriate boundary conditions. The analytical solution for the vertical displacement under the point load is $U_Y = -1.8248 \times 10^{-5}$ mm [87].

Regular mesh: A regular mesh of the type shown in Figure 8(a) is considered first. The vertical displacement directly under the point load, normalized by the same displacement from the analytical solution, is considered for comparison. Figure 8(c) depicts this result for different solid-shell element formulations and for different mesh sizes. It is seen that the element proposed in this paper has good performance for coarse meshes as well as good convergence properties.

Distorted mesh: Next, a 20×20 mesh is considered, with different degrees of distortion represented by an angle θ as shown in Figure 8(b). As the distortion angle θ increases, the mid-surfaces of the



(c) Regular mesh — convergence with mesh refinement

Figure 8. Pinched cylinder with end diaphragms. (a) Regular mesh, (b) distorted mesh and (c) regular mesh — convergence with mesh refinement.

elements become increasingly warped. This typically leads to the membrane locking effect. However, using the ANDES scheme for the membrane response of the element alleviates this membrane locking effect, and results in only mild sensitivity to mesh distortion. Table IV shows that a fairly accurate solution is obtained even for the highly distorted configuration corresponding to $\theta = 40^\circ$.

5.1.3. Scordelis-Lo roof. This is another obstacle course problem originally proposed by Scordelis and Lo [88] for singly curved shells. The goal is to assess the membrane and bending behavior of shell element formulations. As shown in Figure 9, a roof is mounted on two rigid diaphragms at the two curved edges and loaded under self weight. The material behavior is modeled as isotropic linear elastic with $E = 4.32 \times 10^8 \text{ N/mm}^2$ and $\nu = 0$. The roof has radius $R = 25.0 \text{ mm}$, length $L = 50 \text{ mm}$ and thickness $t = 0.25 \text{ mm}$. The specific weight of the material is 360 N/mm^3 . Again, because of symmetry, it is only necessary to represent a quarter of the roof. Boundary conditions corresponding to the rigid diaphragms are given by $U_X = U_Y = 0$. The analytical solution for the vertical displacement of point A under self weight is $U_Y = -0.3024 \text{ mm}$.

The vertical displacement of point A, normalized by this analytical solution, is presented in Table V for different solid-shell formulations. Convergence is satisfactory and occurs from the previous. Unlike the pinched cylinder test, in this problem, the free-edge deflection is dominated by the membrane-bending coupling along the Z direction (bending about the X -axis), along which the elements are not tapered.

5.1.4. Hemispherical shell with 18° hole. This is the third obstacle course problem for doubly-curved shells and assesses the ability of the element to represent inextensional membrane and

Table IV. Pinched cylinder (distorted mesh) – normalized displacement of the point under the load.

Distortion angle (θ)	0°	10°	20°	30°	40°
Normalized displacement	0.970	0.963	0.926	0.925	0.924

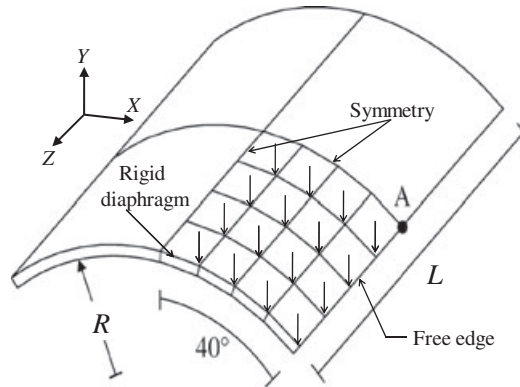


Figure 9. Scordelis-Lo roof model.

Table V. Scordelis-Lo Roof – normalized displacement of point A.

n_e	Present work	Schw09 (Q1STs)	Alv05 (RESS)	Kim05 (XSolid85)	Are03	Sze00 (ANS $_{\gamma\epsilon}$)
4×4	1.047	0.997	0.995	0.960	1.029	0.938
8×8	1.011	0.994	0.986	0.984	1.001	0.962
16×16	0.996	1.000	0.993	0.999	0.992	–
32×32	0.997	1.003	0.996	–	0.991	–

ANS, Assumed Natural Strain.

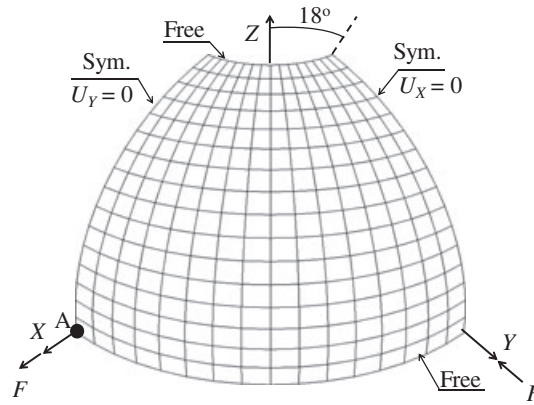


Figure 10. Hemisphere with 18° hole.

Table VI. Hemispherical shell with 18° hole – normalized displacement of point A.

n_e	Present work	Schw09 (Q1STs)	Ree07 (Q1SPs)	Kim05 (XSolid85)	Are03	Kas00 (H1/ME9)	Sze00 (ANS $\gamma\epsilon$ -HS)
4×4	1.018	1.043	0.062	1.058	0.040	0.039	1.062
8×8	0.997	1.002	0.723	1.005	0.756	0.732	1.006
16×16	0.986	0.993	0.919	–	0.991	0.989	–
32×32	0.990	0.994	0.969	–	0.999	0.998	–

ANS, Assumed Natural Strain.

bending modes. The geometry of the model is shown in Figure 10. The radius of the curved shell is $R = 10.0$ mm and the thickness is $t = 0.04$ mm. The model has a hole making an angle $\theta = 18^\circ$ with the Z -axis as shown in the figure. Because of symmetry, only a quadrant of the hemisphere is modeled. The equator represents a free edge, and the XZ and YZ planes are the symmetry planes. The structure is subjected to two pairs of diametrically opposite loads along the X and Y axes, respectively, of magnitude $F = 1.0$ N. The material behavior is modeled as isotropic linear elastic with $E = 6.825 \times 10^7$ N/mm² and $\nu = 0.3$. The computed displacement of node A is normalized by the reference solution $U_X = 0.0940$ mm [86] and presented in Table VI. In comparing convergence of different formulations, ANS-based approaches generally appear to be more effective in circumventing the shear locking problem in thin shells than EAS-based approaches. The present element formulation exhibits good convergence characteristics.

5.1.5. Full hemispherical shell. The model in this example (Figure 11) is identical to that in the previous example, except that it does not have the 18° hole. This is a more demanding test on the formulation because elements are caused to bend about a diagonal plane. The computed displacement of point A, normalized by the reference solution $U_X = 0.0924$ mm [86] is shown in Table VII. The results again demonstrate the excellent convergence characteristics of the proposed element formulation.

5.1.6. Twisted beam. The twisted beam benchmark proposed by MacNeal and Harder [86] is intended to assess the warping performance of the element. The twisted beam shown in Figure 12(a) has length $L = 12$ mm, width $W = 1.1$ mm and thickness $t = 0.32$ mm. Another version of the twisted beam problem, proposed by Simo [9], is shown in Figure 12(b). The only difference is that the latter version has a much smaller thickness of $t = 0.05$ mm and is therefore is a more challenging problem. In both versions, the structure is subjected to two load cases – an in-plane load and an out-of-plane load, both of magnitude $F = 1.0$ N and applied at the tip. The material behavior is

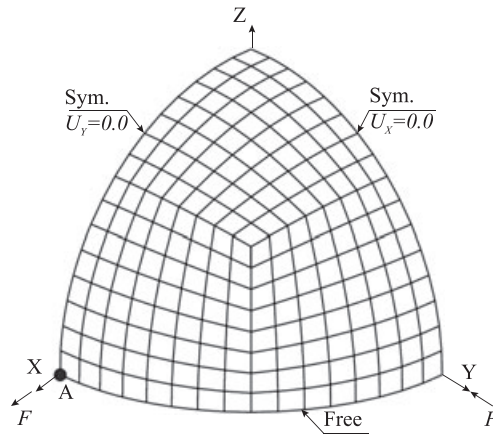
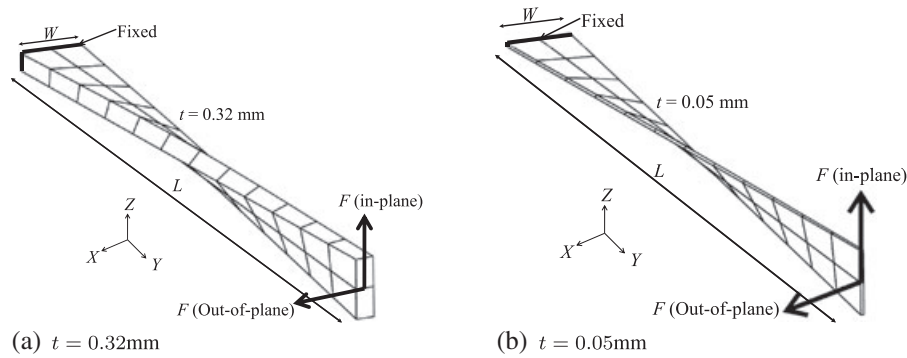


Figure 11. Full Hemisphere problem, geometry.

Table VII. Full hemispherical shell – normalized displacement of point A.

n_e	Present work	Schw09 (Q1STs)	Ree07 (Q1SPs)	Kim05 (XSolid85)	Gru05	Are03	Car02
4	0.663	0.418	0.104	–	0.573	0.029	0.680
8	0.962	0.956	0.630	1.079	0.971	0.583	0.980
16	0.997	0.996	0.907	1.014	1.002	0.978	0.990
32	1.002	0.999	0.970	1.000	1.000	0.999	–

Figure 12. Twisted Beam. (a) $t = 0.32$ mm; and (b) $t = 0.05$ mm.

modeled as isotropic linear elastic with $E = 29 \times 10^6$ N/mm² and $\nu = 0.22$. The tip displacements in the direction of loading are taken for comparison and normalized by the reference analytical solutions. Results are presented in Tables VIII–XI. The proposed element formulation results in excellent performance even in a highly warped thin-beam configuration.

5.1.7. Clamped square plate. This test assesses sensitivity of the element to distortion. The geometry is shown in Figure 13(a). The side length is $L = 100$ mm and the thickness is $t = 1$ mm. The material behavior is modeled as isotropic linear elastic with $E = 10^4$ N/mm² and $\nu = 0.3$. A concentrated force of magnitude $F = 16.3527$ N is applied at the center of the plate in the negative Z direction. Owing to symmetry, only a quarter of the plate is modeled. The plate is discretized using four elements as depicted in Figure 13(a), and element distortion is varied changing the location of the point A in the range $0 \leq e \leq 12$ mm. The analytical solution for this problem is given by [89]

$$U_Z = 0.00560 FL^2 \frac{12(1-\nu^2)}{Et^3} = -1.000 \text{ mm} \quad (60)$$

Table VIII. Twisted thin beam – in-plane load (reference solution = 1.387 mm).

n_e	Present work	Schw09 (Q1STs)	Car08 (MRESS)	Alv05 (RESS)	Simo89
6×1	1.005	1.002	–	–	0.993
12×2	1.001	0.998	0.965	0.998	1.000
24×4	1.000	0.999	1.000	1.000	1.001
48×8	1.000	1.000	1.001	1.000	1.002

Table IX. Twisted thin beam – out-of-plane load (reference solution = 0.343 mm).

n_e	Present work	Schw09 (Q1STs)	Car08 (MRESS)	Alv05 (RESS)	Simo89
6×1	0.953	0.942	–	–	0.951
12×2	0.988	0.983	0.958	0.985	0.986
24×4	0.995	0.995	0.995	0.996	0.997
48×8	1.000	0.999	0.999	0.998	1.000

Table X. Twisted thick beam – in-plane load (reference solution = 0.005424 mm).

n_e	Present work	Car08 (MRESS)	Alv05 (RESS)	Sze00 (ANS $_{\gamma\epsilon}$)	Sze00 (ANS $_{\gamma\epsilon}$)-HS
6×1	0.996	–	–	0.934	0.998
12×2	0.997	1.002	0.994	0.945	1.001
24×4	0.999	1.000	0.996	–	–
48×8	1.000	1.000	0.997	–	–

ANS, Assumed Natural Strain.

Table XI. Twisted thick beam – out-of-plane load (reference solution = 0.001754 mm).

n_e	Present work	Car08 (MRESS)	Alv05 (RESS)	Sze00 (ANS $_{\gamma\epsilon}$)	Sze00 (ANS $_{\gamma\epsilon}$)-HS
6×1	0.946	–	–	0.780	0.957
12×2	0.987	1.022	0.935	0.887	0.990
24×4	0.995	1.006	0.979	–	–
48×8	0.999	1.002	0.992	–	–

ANS, Assumed Natural Strain.

The displacement at the center is normalized with respect to the analytical solution and plotted versus the distortion parameter e in Figure 13(b). All element formulations considered exhibit satisfactory performance under significant distortion. This can be attributed to the fact that they all use the ANS approach to circumvent the shear locking problem. The formulation proposed in [21] behaves slightly better than the others in a highly distorted configuration.

5.1.8. Cook's skew plate. This test was proposed by Cook [90] and applied to shell formulations by Simo [9]. The goal is to assess the membrane behavior of the element. As shown in Figure 14(a), a trapezoidal beam is clamped at one end and subject to a uniformly distributed shear traction of total magnitude $F = 1/16$ at the tip. The material behavior is modeled as isotropic linear elastic with $E = 1.0$ and $\nu = 1/3$. The thickness of the model is $t = 1.0$.

The analytical solution for this problem is $U_Y^A = 23.91$. The computed vertical displacement of point A in Figure 14(b). For coarse discretizations, the element proposed here shows better performance than most other solid-shell formulations considered. The iCYSE-E4 shell formulation with four enhanced strain variables [75] has better convergence rate, although it does not pass the membrane patch test.

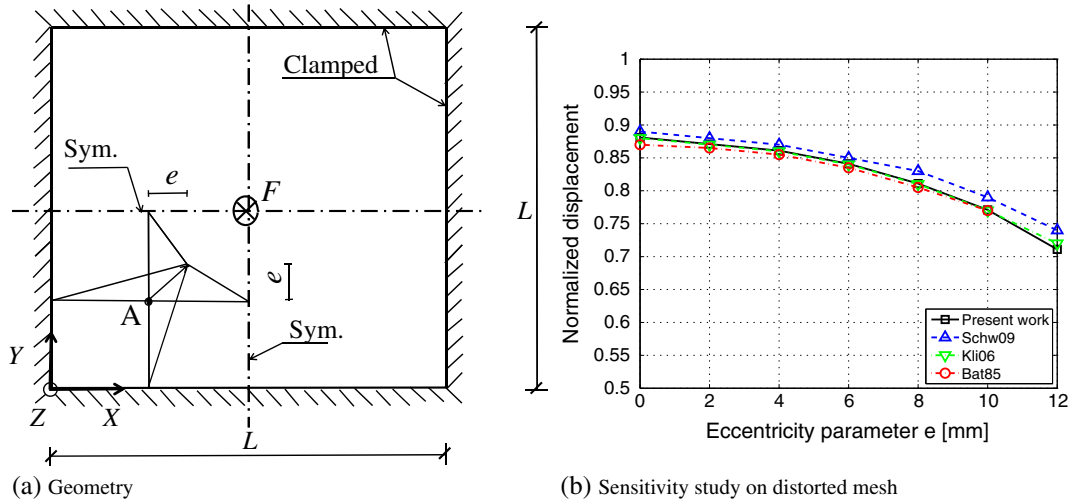


Figure 13. Clamped Square Plate. (a) Geometry and (b) sensitivity study on distorted mesh.

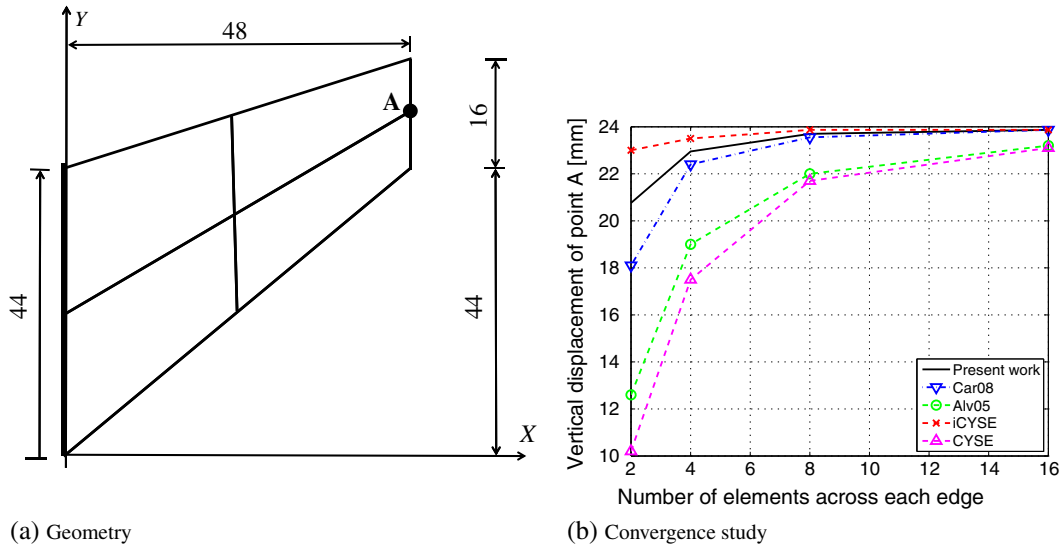


Figure 14. Cook's skew plate. (a) Geometry and (b) convergence study.

5.2. Geometrically nonlinear benchmark problems

In this subsection, some geometrically nonlinear problems are investigated. Material behavior is taken to be isotropic linear elastic. The *arc length* method originally proposed by Riks [91] with *orthogonal trajectory iterations* [92] for the correction phase is used as the solution algorithm with a convergence tolerance of 10^{-7} on the Euclidean norm of the force residual vector.

5.2.1. Buckling of a square plate. In this example, the goal is to compute the buckling and post-buckling behavior of a plate under in-plane uniaxial compression. The plate dimensions are $508 \times 508 \times 3.175$ mm as shown in Figure 15(a). Material properties are $E = 2.062 \times 10^5$ N/mm² and $\nu = 0.30$. Because of symmetry, only a quarter of the plate is modeled. The outer edges are restrained from out-of-plane translation. A uniform compressive force of N_X per unit length is applied along edges $X = 0$ and $X = L$. The analytical solution for the critical buckling load is [93]

$$(N_X)_{cr} = \frac{\pi^2 D}{L^2} \left(m + \frac{1}{m} \right)^2 \quad \text{where } D = \frac{Et^3}{12(1 - \nu^2)} \quad (61)$$

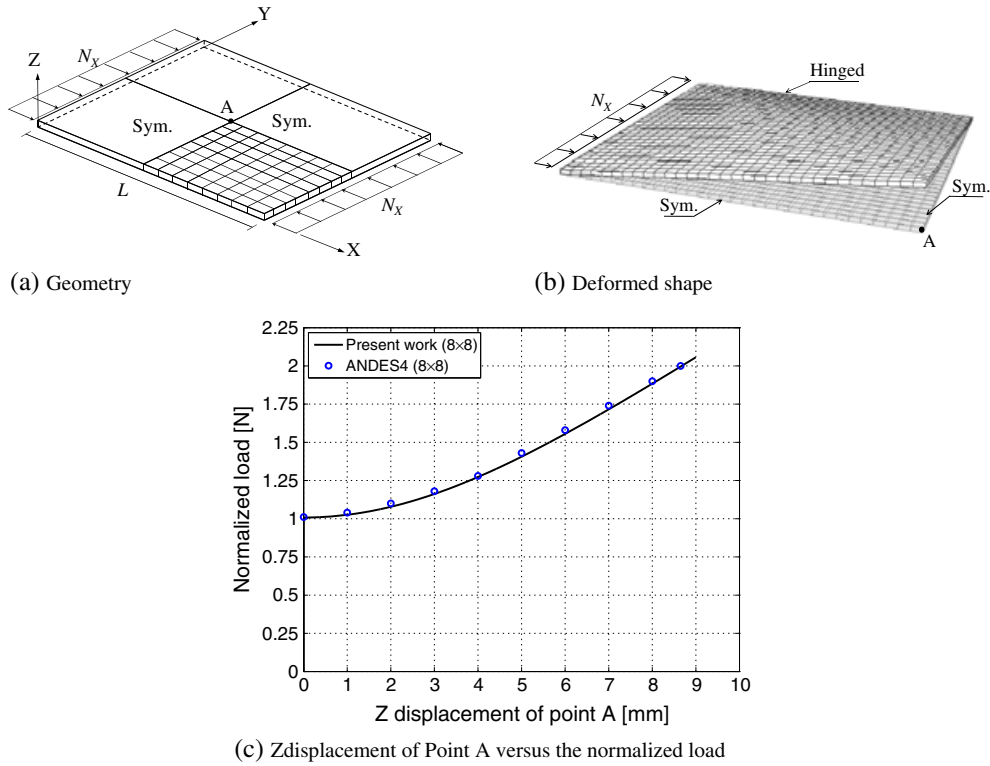


Figure 15. Buckling analysis of square plate compressed in one direction. (a) Geometry, (b) deformed shape and (c) Z displacement of Point A versus the normalized load.

Table XII. Buckling load for square plate subjected to compression.

n_e	Present work	ANDES3	ANDES4
4×4	1.022	1.008	1.043
8×8	1.003	1.002	1.011
16×16	1.000	1.000	1.002
32×32	1.000	1.000	1.001

where m is the number of half-waves in the compression direction. $m = 1$ for the first buckling mode. An initial imperfection is imposed on the model by applying a force at point A in Z direction of magnitude 0.0003% of the critical buckling load.

Numerical results, normalized to the analytical critical buckling load $(N_x)_{cr} = 92.455$ N/mm, are shown in Table XII. Results are compared with existing shell formulations, ANDES3 and ANDES4, which also use the CR approach for nonlinear kinematics [52]. It is observed that performance of the triangular ANDES3 element is slightly better than that of the proposed element for the coarse mesh, because in this case, there are twice as many triangular elements as quadrilateral elements and hence results in better approximation with the CR description. The proposed solid-shell element, however, converges faster than the quadrilateral ANDES4 element. Post-buckling behavior is shown in Figure 15(c) and the deformed shape in Figure 15(b).

5.2.2. Pinching of a clamped cylinder: In this test, a cantilevered cylinder is subjected to a pair of opposing loads at its open end as shown in Figure 16(a). This is a demanding test for solid-shell elements because they are prone to trapezoidal locking when modeling curved geometries. The radius of the cylinder, $R = 1.016$ mm, the length, $L = 3.048$ mm and the thickness, $t = 0.03$ mm. Material parameters are $E = 2.0685 \times 10^7$ N/mm² and $\nu = 0.30$. Owing to symmetry, only a quarter of the structure is modeled. The total load $F = \lambda F_0$ with λ , a load multiplier and $F_0 = 1600$ N is

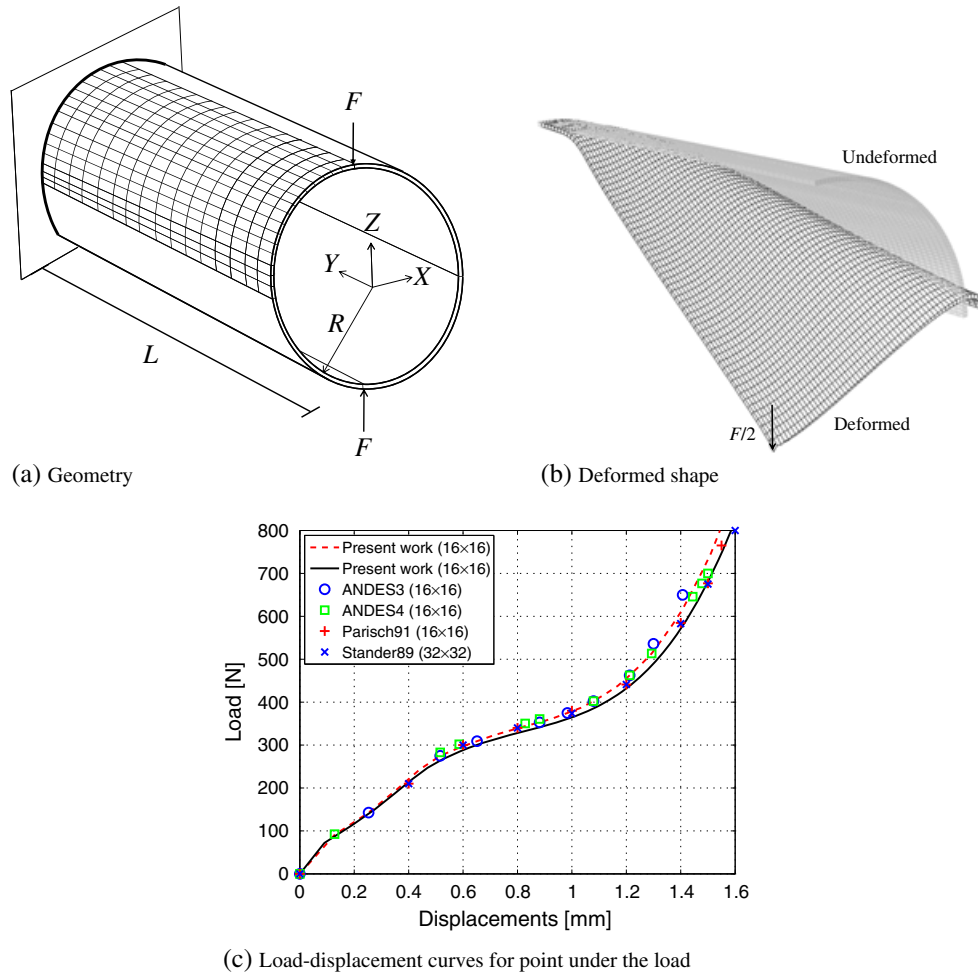


Figure 16. Pinching of a clamped cylinder. (a) Geometry, (b) deformed shape and (c) load-displacement curves for point under the load.

applied in 20 equal increments, until the tip displacement reaches 1.6 times the radius of the cylinder (although only displacements up to the radius are physically meaningful). On average, 6–12 iterations are required at each corrector step.

Numerical results are shown in Figure 16(c) together with those from some existing shell formulations (ANDES3, ANDES4, Stander89, Parisch91). The ANDES3 solution with a 16 mesh diverges before target displacement is reached. Results also show that the solid-shell produces slightly stiffer solution than other shell formulations for a 16 mesh. This is due to trapezoidal locking. A regular 24×24 mesh arrangement, however, shows very good agreement with the published solutions, especially Stander89 with a regular 32×32 mesh. The deformed configuration at the target displacement is shown in Figure 16(b).

5.2.3. Stretching of a cylinder with free ends. In this test, an open cylinder with free ends is subjected to two diametrically opposite forces at half-length as shown in Figure 17(a). The radius of the cylinder $R = 4.935$ mm, length $L = 10.35$ mm and the thickness $t = 0.094$ mm. Materials parameters, $E = 10.5 \times 10^6$ N/mm² and $\nu = 0.3125$. The load $F = 40.0$ kN. Because of symmetry, only one octant of the cylinder is modeled. Large rotations occur involving both membrane and bending responses. Different mesh arrangements using both solid-shell [44, 46, 49] and conventional shell [94, 95] elements have been explored in the literature, all addressing large deformations.

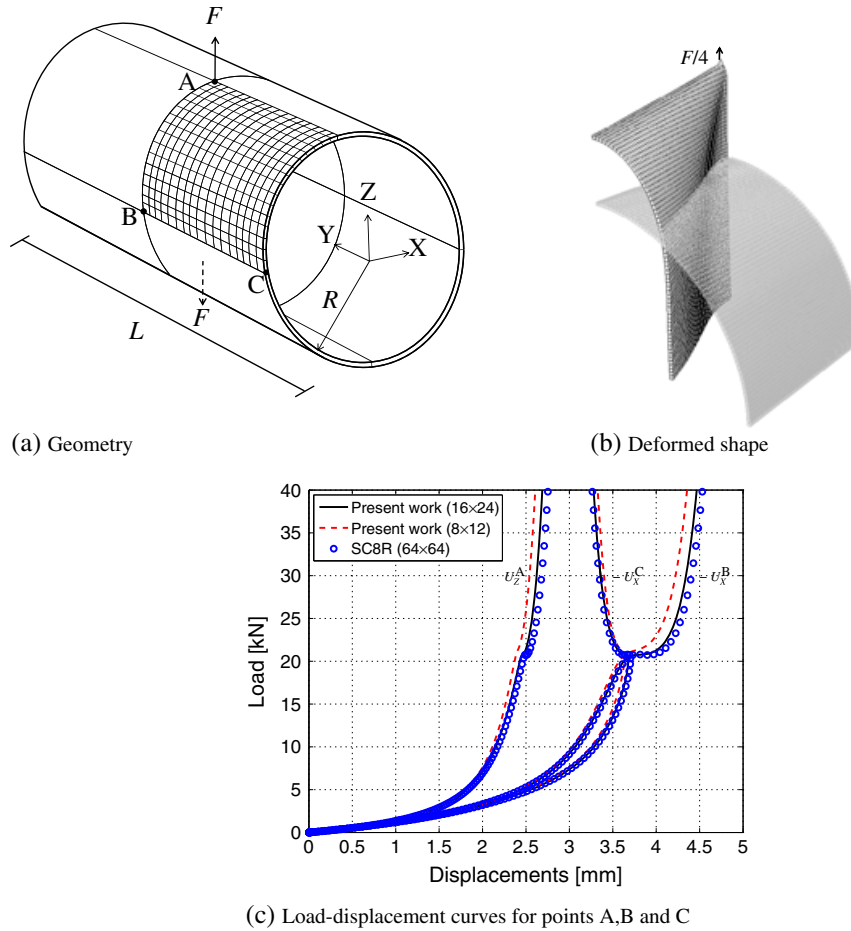


Figure 17. Stretching of a cylinder with free ends. (a) Geometry, (b) deformed shape and (c) load-displacement curves for points A, B and C.

Here, we use 8×12 and 16×24 meshes to model one octant of the cylinder. The Z -displacements of points A, B and C shown in Figure 17(a) are plotted in Figure 17(c). A solution obtained using a fine mesh (64×64) of SC8R elements in ABAQUS is used as the reference solutions. The results in Figure 17(c) show that the response has two regimes: (i) a primary phase dominated by bending effects and characterized by large rotations, where the cylinder is stretched uniformly until the load reaches a value $F = 21.0$ kN; and (ii) a secondary phase dominated by membrane effects characterized by large deformational displacements, when a snap-through occurs and the model exhibits an abrupt increase in displacements. Using a coarse mesh with 8×12 elements, the snap-through occurs at the same load level as the reference solution and the displacement of point A at load $F = 40.0$ kN is 95% of the reference displacement. This illustrates how the ANDES formulation performs satisfactorily in alleviating membrane locking. Using a fine mesh with 16×24 elements, the displacement of point A at load level $F = 40.0$ kN is 99.4% of the reference solution. As reported in [49], the computed Green strains at the maximum load level are in order of 10%, which fall in the context of large deformations. By using the present formulation, an accurate solution is obtained with only seven equal increments. Nonetheless, to display smooth curves, 60 equal increments are used for plotting. The number of corrector iterations for the first 10 increments are presented in Table XIII. The deformed configuration at the maximum load value is shown in Figure 17(b).

5.2.4. Clamped-hinged deep circular arch subjected to a concentrated load. This example is from [46] and [96]. A deep circular arch hinged at one end and clamped at the other is subjected to a

Table XIII. Stretching of a cylinder, iterations for the first 10 increments.

No. of increments			No. of iterations							
7	5	6	6	8	8	11	14	–	–	–
60	3	3	3	3	3	3	3	4	4	3

point load at its apex as is shown in Figure 18(a). The radius of the arch, $R = 100$ mm, thickness $t = 1$ mm and width $w = 24$ mm. The material properties are $E = 0.5 \times 10^5$ N/mm² and $\nu = 0.0$. The arch is meshed with 40×1 elements, and 50 equal increments are used for the nonlinear analysis. The X and Y displacements of the point under the load are plotted in Figure 18(c) together with results from [46] obtained using SHB8PS. The deformed shape of the arch is shown in Figure 18(b). The response obtained using the current solid-shell element with CR kinematics conforms with that from [46]) computed using an updated Lagrangian approach. The peak load is slightly different (990N vs. 950N).

5.2.5. Twisted beam under out-of-plane loading. In this test, the performance of the nonlinear formulation is assessed when the geometry is warped. The model, shown in Figure 12(b), is identical to the one used in example 5.1.6 with thickness $t = 0.05$ mm. An out-of-plane load is applied at the free end of the beam at point A. A version of this problem with $t = 0.032$ mm has been studied in the literature [46, 97] with mesh arrangements of 12×2 , 24×4 and 48×4 . Here, a 24×4 mesh

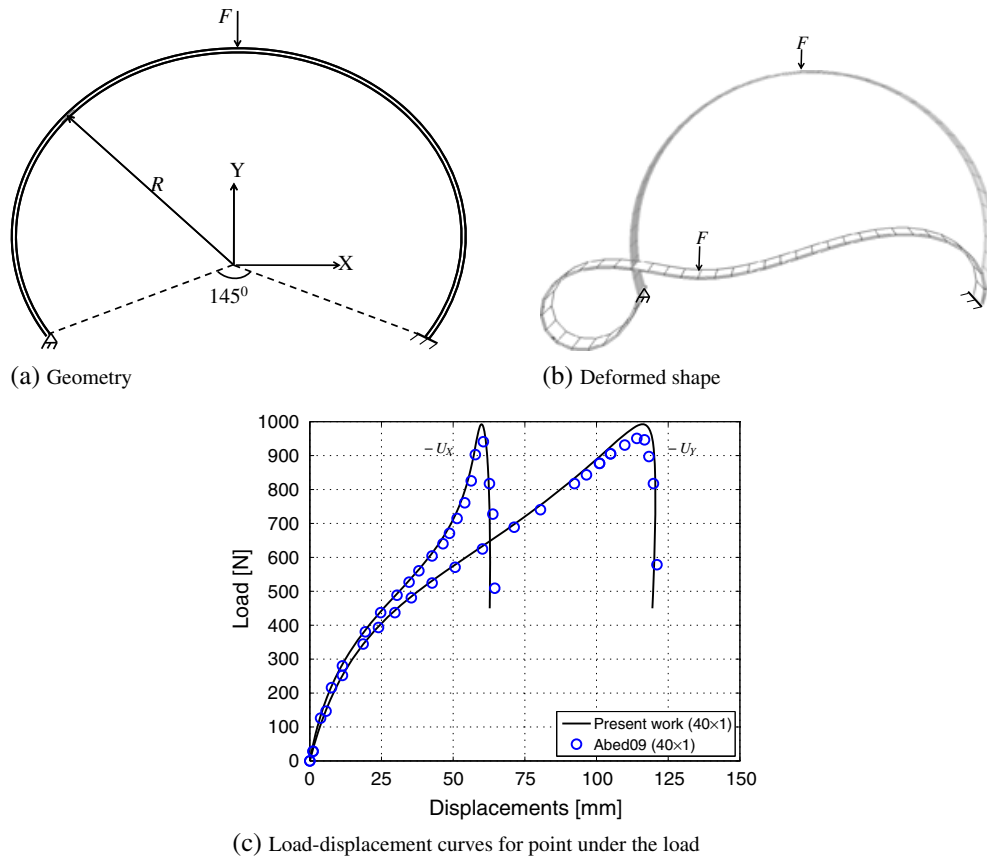


Figure 18. Clamped-hinged deep circular arch subjected to a concentrated load. (a) Geometry, (b) deformed shape and (c) load-displacement curves for point under the load.

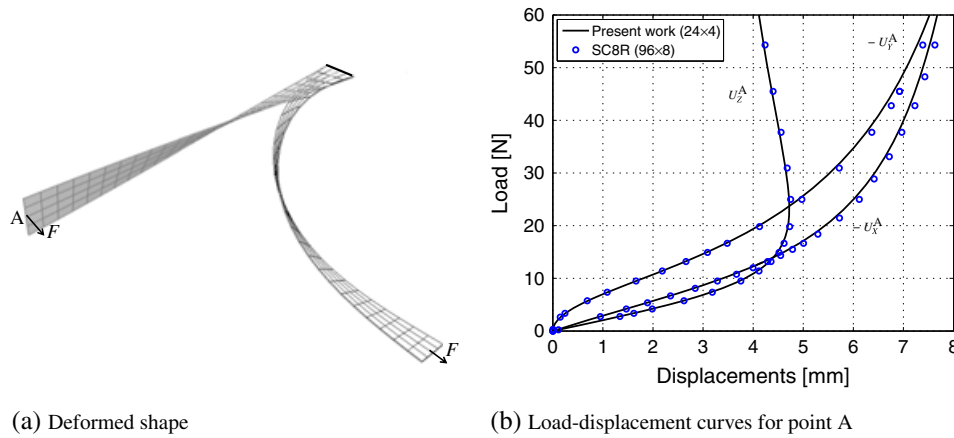


Figure 19. Twisted beam under out-of-plane loading. (a) Deformed shape and (b) load-displacement curves for point A.

is considered, and 15 increments are used. A reference solution is computed using fine mesh with 96×8 SC8R elements in ABAQUS.

The X , Y and Z displacements of point A are plotted in Figure 19(b) along with the reference solution. The relatively coarse mesh of solid-shell elements employing CR kinematics agrees with the reference solution that uses an updated Lagrangian approach. The deformed shape of the twisted beam is shown in Figure 19(a). It is noted that when an even coarser mesh with 6×1 is used, the model becomes stiff and the results diverge from the reference solution for large displacements, even though the linear problem shows excellent agreement with the analytical solution for coarse meshes. This locking problem under geometrically nonlinearity is because when the solid-shell element is highly warped, the corotated frame is not optimum, that is, considering a frame that travels with the mid-surface is not an optimum frame.

5.2.6. Slit annular plate subjected to lifting line force. This is another benchmark used to assess the performance of thin-shell formulations under finite rotations. It was first proposed in [98] and [99] and subsequently adopted by other authors [46, 95, 97]. The model consists of a circular ring as shown in Figure 20(a), with a slit in the radial direction along A and B. The internal and external radii of the ring are $R_i = 6$ mm and $R_e = 10$ mm, respectively, and its thickness is $t = 0.03$ mm. The material properties used are $E = 21 \times 10^6$ N/mm² $\nu = 0.0$. A vertical lifting line force is applied on one edge of the slit, and the other edge is fully clamped.

Different mesh arrangements have been used in the literature in the context of this problem, such as 6×48 , 8×64 and 10×80 with one element across the thickness. In [95], this problem has been studied with two meshes of 6×30 and 10×80 using the S4R shell element. This reference is selected to compare the results. Following Abed-Meraim and Combescure [46], in the current work, an intermediate mesh of 8×64 is used. Twenty equal increments are used to plot the response curve, although accurate results are obtained with only 10 increments. Vertical displacements of points A and B are plotted in Figure 20(c) along with the reference solution. The results of solid-shell formulation with CR kinematics conform with the reference solution, which uses an updated Lagrangian approach. The deformed shape of the ring is also shown in Figure 20(b), which shows the large displacement and rotation of the free edge.

5.2.7. Hinged cylindrical shell under concentrated load. This is a common test to assess the path following algorithm. The model is a segment of a cylindrical shell hinged at the two edges and subjected to a concentrated load (Figure 21(a)). The radius of the cylinder is $R = 2540$ mm, the length $L = 508$ mm and the angle made by the segment at the center, $\theta = 0.1$ rad. Because of symmetry, only a quarter of the structure is modeled. Material properties used are $E = 3102.75$ N/mm² and $\nu = 0.3$.

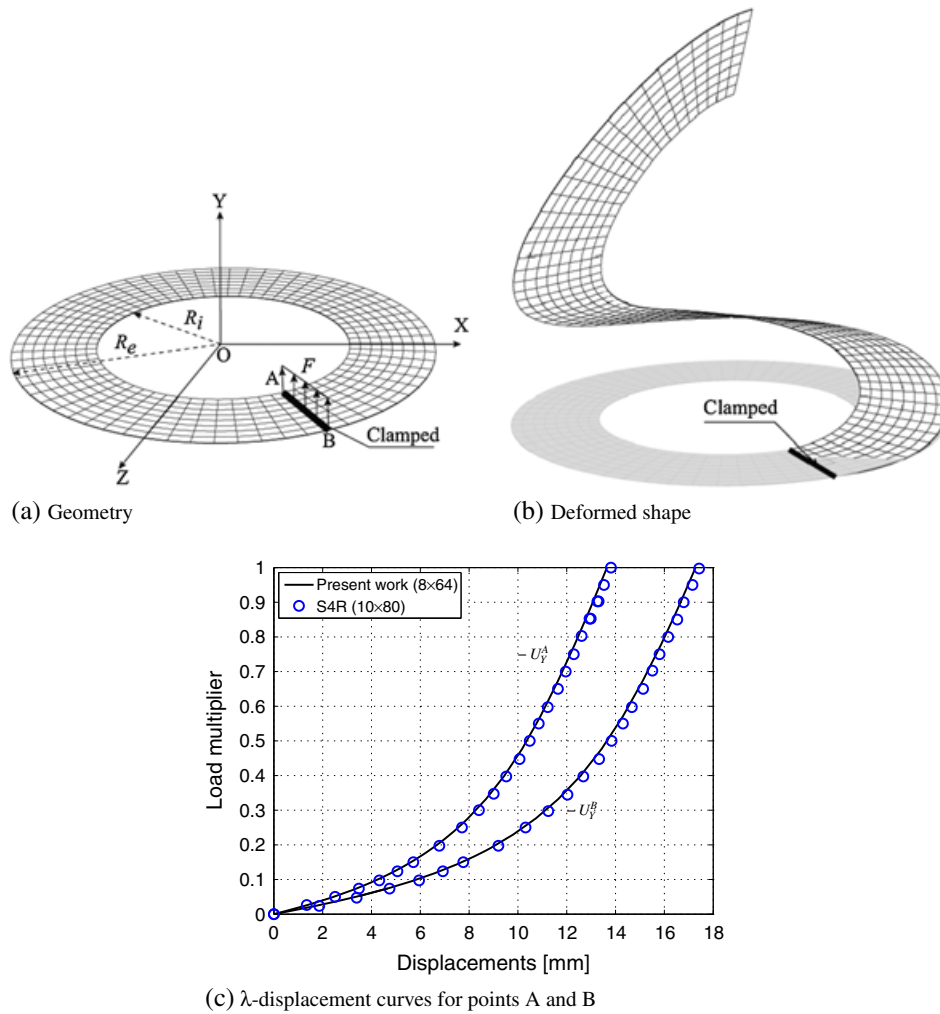


Figure 20. Slit annular plate subjected to lifting line force. (a) Geometry, (b) deformed shape and (c) λ -displacement curves for points A and B.

Two versions of this problem have been utilized in the literature. Areias *et al.*, Cardoso *et al.* and Alves de Sousa *et al.* [24, 26, 48] consider a thin shell with thickness $t = 6.35$ mm, and Legay and Combescure [100], a thick shell with $t = 12.70$ mm. Both cases are examined in [28, 44, 95, 101]. In this work, we analyze the thin version, which is perhaps a more challenging problem. Sze *et al.* [95] studied this problem by using meshes of 16×16 and 24×24 S4R shell elements in ABAQUS. The coarsest mesh that has been used for this problem in the literature is 4×4 in [21, 101]. In the present work, this coarse 4×4 mesh is used. A solution computed using a 64×64 mesh of S4R elements in ABAQUS is used as the reference. Results are also compared with those from Schwarz and Reese [21] using a 4×4 mesh of Q1ST elements. Following common practice when using solid-shell elements, to represent the hinged support, the thickness is discretized with two elements, which allows fixing the translational DOF of the mid-plane edge nodes.

Vertical displacements of points A and B are plotted in Figure 21(c). In general, the results show good agreement with the reference solution. The current solid-shell is slightly more flexible than the reference solution after snap-back occurs. Fifteen equal increments are used for the analysis. The norm of the force residual is shown in Table XIV. Fifty increments are used for the plots in Figure 21(c).

Following Legay and Combescure [100] who investigated the sensitivity of results to boundary conditions for the thick-shell version ($t = 12.70$ mm), we explore the effect of applying

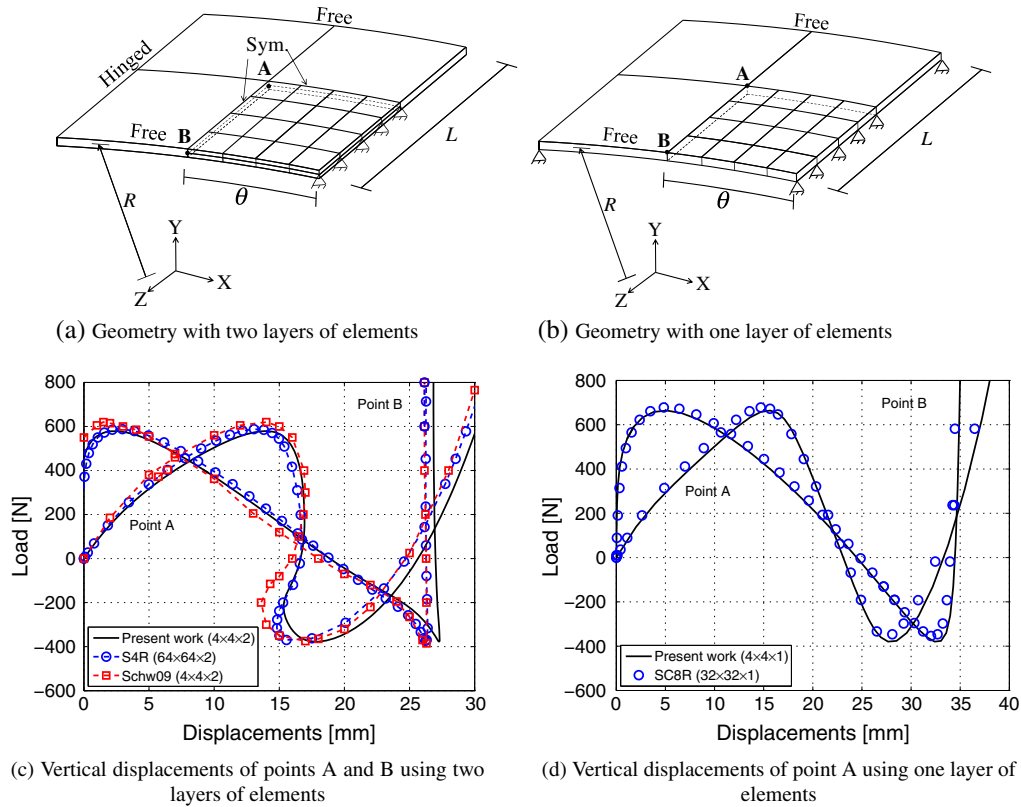


Figure 21. Hinged cylinder problem. (a) Geometry with two layers of elements, (b) geometry with one layer of elements, (c) vertical displacements of points A and B using two layers of elements and (d) vertical displacements of point A using one layer of elements.

Table XIV. Hinged cylinder problem with two layers of elements – Euclidean norm of the force residual vector for corrector iterations.

Iteration	1	4	Increment 7	11	15
1	23216.743	9761.246	14231.813	18395.300	15945.004
2	77.696	545.538	121.114	568.035	33.166
3	7.113	69.277	17.690	368.732	0.726
4	1.862×10^{-4}	0.266	5.152×10^{-3}	3.243	7.241×10^{-7}
5	1.823×10^{-8}	2.586×10^{-5}	3.368×10^{-8}	3.896×10^{-3}	4.213×10^{-10}
6		2.424×10^{-8}		3.180×10^{-8}	

the support conditions at the lower edge instead of at the mid-plane level. For this, we discretize the model with one layer of elements as shown in Figure 21(b). The ensuing displacements of point A are plotted in Figure 21(d) together with results from $32 \times 32 \times 1$ mesh of SC8R elements in ABAQUS used as a reference solution. The snap-back response that appeared when the model was hinged at mid-plane level now vanishes, and the larger deformations are found to occur.

6. CONCLUDING REMARKS

A solid-shell finite element based on an assumed strain approach has been presented. The kinematic decomposition separates the element behavior into in-plane, transverse shear and thickness components. These three components are constructed using variants of the generic assumed strain

approach. The ANDES variant, which is a hybrid of the Free Formulation and ANS approaches, is used to construct the in-plane strain field. For the out-of-plane transverse shear and thickness components, the assumed strain field is constructed by evaluating the compatible strain at collocation points, followed by interpolation. In addition, the thickness strain is enhanced to represent linear variation associated with out-of-plane bending. When applied to highly warped elements, the in-plane formulation is found to result in nonzero strains when the element is displaced as a rigid body. As a result, a projector is used to filter rigid body displacements. Full Gauss quadrature is used on all components to produce the element stiffness matrix; as a result, the well-known rank deficiency problems associated with reduced and selective integration are avoided.

The resulting element is subjected to a number of well-known benchmark tests for shell elements. These challenge different aspects of the element formulation, including its performance under mesh distortion, warped mesh arrangements, and single and doubly curved geometries. Special attention is placed on the various locking phenomena discussed in Section 1. The element performs well in all of these cases; in particular, it passes both membrane and (higher order) bending patch tests. In Cook's skew-plate benchmark that tests in-plane behavior, the proposed solid-shell formulation exhibits very good convergence rate compared with other solid-shell formulations in the literature. The pinched cylinder model with end diaphragms shows that the thickness tapered elements may suffer from poor convergence rate for inextensional bending problems. However, this benchmark shows that the current linear element formulation results in relatively accurate solutions even with coarser meshes compared with other cited shell and solid-shell formulations.

The element formulation has been extended to the geometric nonlinear regime using the element-independent CR approach. The nonlinear element has been subjected to different benchmarks that involve geometric nonlinear effects such as post-buckling behavior, snap-through and snap-back phenomena. Numerical results illustrate that in the small-strain context, and considering similar mesh discretizations, the present formulation based on the CR kinematic description works as well as the other nonlinear elements based on the Updated Lagrangian or Total Lagrangian kinematic descriptions in terms of convergence rates to reference solutions.

ACKNOWLEDGEMENT

The first and second authors gratefully acknowledge financial support from the National Science Foundation through the grant CMMI-0847053.

REFERENCES

1. Betsch P, Gruttmann F, Stein E. A 4-node finite shell element for the implementation of general hyperelastic 3D-elasticity at finite strains. *Computer Methods in Applied Mechanics and Engineering* 1996; **130**(1–2):57–79.
2. Bischoff M, Ramm E. Shear deformable shell elements for large strains and rotations. *International Journal for Numerical Methods in Engineering* 1997; **40**(23):4427–4449.
3. Brank B, Korelc J, Ibrahimbegovic A. A. Nonlinear shell problem formulation accounting for through-the-thickness stretching and its finite element implementation. *Computers and Structures* 2002; **80**(9–10):699–717.
4. Cardoso RPR, Yoon JW. One point quadrature shell element with through-thickness stretch. *Computer Methods in Applied Mechanics and Engineering* 2005; **194**(9–11):1161–1199.
5. Lu H, Ito K, Kazama K, Namura S. Development of a new quadratic shell element considering the normal stress in the thickness direction for simulating sheet metal forming. *Journal of Materials Processing Technology* 2006; **171**(3):341–347.
6. Belytschko T, Lin JJ, Tsay CS. Explicit algorithms for the nonlinear dynamics of shells. *Computer Methods in Applied Mechanics and Engineering* 1984; **42**(2):225–251.
7. Bathe KJ, Dvorkin EN. A four-node plate bending element based on Mindlin/Reissner plate theory and a mixed interpolation. *International Journal for Numerical Methods in Engineering* 1985; **21**(2):367–383.
8. Park KC, Stanley GM. A curved C0 shell element based on assumed natural-coordinate strains. *Journal of Applied Mechanics-Transactions of the ASME* 1986; **53**(2):278–290.
9. Simo JC, Fox DD. On a stress resultant geometrically exact shell model. I. Formulation and optimal parametrization. *Computer Methods in Applied Mechanics and Engineering* 1989; **72**(3):267–304.
10. Simo JC, Rifai MS, Fox DD. On a stress resultant geometrically exact shell model. IV. Variable thickness shells with through-the-thickness stretching. *Computer Methods in Applied Mechanics and Engineering* 1990; **81**(1):91–126.
11. Simo JC, Kennedy JG. On a stress resultant geometrically exact shell model. V. Nonlinear plasticity: formulation and integration algorithms. *Computer Methods in Applied Mechanics and Engineering* 1992; **96**(2):133–171.

12. César de Sá JMA, Natal Jorge RM, Fontes Valente RA, Almeida Areias PM. Development of shear locking-free shell elements using an enhanced assumed strain formulation. *International Journal for Numerical Methods in Engineering* 2002; **53**(7):1721–1750.
13. Buechter N, Ramm E. Shell theory versus degenerationa comparison in large rotation finite element analysis. *International Journal for Numerical Methods in Engineering* 1992; **34**(1):39–59. DOI: 10.1002/nme.1620340105.
14. Cirak F, Ortiz M, Schröder P. Subdivision surfaces: a new paradigm for thin-shell finite-element analysis. *International Journal for Numerical Methods in Engineering* 2000; **47**(12):2039–2072.
15. Cirak F, Ortiz M. Fully c1-conforming subdivision elements for finite deformation thin-shell analysis. *International Journal for Numerical Methods in Engineering* 2001; **51**(7):813–833. DOI: 10.1002/nme.182.
16. Parisch H. A continuum-based shell theory for non-linear applications. *International Journal for Numerical Methods in Engineering* 1995; **38**(11):1855–1883.
17. Miehe C. A theoretical and computational model for isotropic elastoplastic stress analysis in shells at large strains. *Computer Methods in Applied Mechanics and Engineering* 1998; **155**(3–4):193–233.
18. Hauptmann R, Schweizerhof K. Systematic development of ‘solid-shell’ element formulations for linear and non-linear analyses employing only displacement degrees of freedom. *International Journal for Numerical Methods in Engineering* 1998; **42**(1):49–69.
19. Hauptmann R, Schweizerhof K, Doll S. Extension of the solid-shell concept for application to large elastic and large elastoplastic deformations. *International Journal for Numerical Methods in Engineering* 2000; **49**(9):1121–1141.
20. Sze KY. Three-dimensional continuum finite element models for plate/shell analysis. *Progress in Structural Engineering and Materials* 2002; **4**(4):400–407. DOI: 10.1002/pse.133.
21. Schwarze M, Reese S. A reduced integration solid-shell finite element based on the EAS and the ANS concept-Geometrically linear problems. *International Journal for Numerical Methods in Engineering* 2009; **80**(10):1322–1355.
22. Alves de Sousa RJ, Natal Jorge RM, Fontes Valente RA, César de Sá JMA. A new volumetric and shear locking-free 3D enhanced strain element. *Engineering Computations* 2003; **20**(7):896–925.
23. Andelfinger U, Ramm E. EAS-elements for two-dimensional, three-dimensional, plate and shell structures and their equivalence to HR-elements. *International Journal for Numerical Methods in Engineering* 1993; **36**(8):1311–1337.
24. Areias PMA, César de Sá JMA, Conceição António CA, Fernandes AA. Analysis of 3D problems using a new enhanced strain hexahedral element. *International Journal for Numerical Methods in Engineering* 2003; **58**(11):1637–1682.
25. Fontes Valente RA, Alves De Sousa RJ, Natal Jorge RM. An enhanced strain 3D element for large deformation elastoplastic thin-shell applications. *Computational Mechanics* 2004; **34**(1):38–52.
26. Cardoso RPR, Yoon JW, Mahardika M, Choudhry S, Alves de Sousa RJ, Fontes Valente RA. Enhanced assumed strain (EAS) and assumed natural strain (ANS) methods for one-point quadrature solid-shell elements. *International Journal for Numerical Methods in Engineering* 2008; **75**(2):156–187.
27. Felippa CA. The SS8 solid shell element: A Fortran implementation. *Report CU-CAS-02-04*, Center for Aerospace Structures, College of Engineering, University of Colorado, March 2002.
28. Kim KD, Liu GZ, Han SC. A resultant 8-node solid-shell element for geometrically nonlinear analysis. *Computational Mechanics* 2005; **35**(5):315–331.
29. Sze KY, Yao LQ. A hybrid stress ANS solid-shell element and its generalization for smart structure modelling. Solid-shell element formulation. *International Journal for Numerical Methods in Engineering* 2000; **48**(4):545–564.
30. Vu-Quoc L, Tan XG. Optimal solid shells for non-linear analyses of multilayer composites. I. Statics. *Computer Methods in Applied Mechanics and Engineering* 2003; **192**(9–10):975–1016.
31. Wagner W, Klinkel S, Gruttmann F. A robust non-linear solid shell element based on a mixed variational formulation. *Computer Methods in Applied Mechanics and Engineering* 2006; **195**(1–3):179–201.
32. Betsch P, Stein E. An assumed strain approach avoiding artificial thickness straining for a non-linear 4-node shell element. *Communications in Numerical Methods in Engineering* 1995; **11**(11):899–909.
33. MacNeal RH. Simple quadrilateral shell element. *Computers and Structures* 1978; **8**(2):175–183.
34. Dvorkin EN, Bathe KJ. Continuum mechanics based four-node shell element for general non-linear analysis. *Engineering Computations* 1984; **1**(1):77–88.
35. Felippa CA, Militello C. Membrane triangles with corner drilling freedoms – II. The ANDES element. *Finite Elements in Analysis and Design* 1992; **12**(3–4):189–201.
36. Militello C, Felippa CA. First ANDES elements: 9-DOF plate bending triangles, (Final report, December 1989). *Technical Report*, 1991.
37. Bergan PG. Finite elements based on energy orthogonal functions. *International Journal for Numerical Methods in Engineering* 1980; **15**(10):1541–1555.
38. Bergan PG, Nygard MK. Finite elements with increased freedom in choosing shape functions. *International Journal for Numerical Methods in Engineering* 1984; **20**(4):643–663.
39. Bergan PG, Felippa CA. A triangular membrane element with rotational degrees of freedom. *Computer Methods in Applied Mechanics and Engineering* 1985; **50**(1):25–69.
40. Felippa CA, Bergan PG. A triangular bending element based on an energy-orthogonal free formulation. *Computer Methods in Applied Mechanics and Engineering* 1987; **61**(2):129–160.

41. Nygard M. The free formulation for nonlinear finite elements with application to shells. *Ph.D. Thesis*, Norwegian Institute of Technology, 1986.
42. Simo JC, Hughes TJR. On the variational foundations of assumed strain methods. *Journal of Applied Mechanics-Transactions of the ASME* 1986; **53**(1):51–54.
43. Rankin CC, Nour-Omid B. The use of projectors to improve finite element performance. *Computers and Structures* 1988; **30**(1–2):257–267.
44. Schwarze M, Reese S. A reduced integration solid-shell finite element based on the EAS and the ANS concept-Large deformation problems. *International Journal for Numerical Methods in Engineering*; **85**(3):289–329.
45. Abed-Meraim F, Combescure A. SHB8PS-a new adaptative, assumed-strain continuum mechanics shell element for impact analysis. *Computers and Structures* 2002; **80**(9–10):791–803.
46. Abed-Meraim F, Combescure A. An improved assumed strain solid-shell element formulation with physical stabilization for geometric non-linear applications and elastic-plastic stability analysis. *International Journal for Numerical Methods in Engineering* 2009; **80**(13):1640–1686.
47. Alves de Sousa RJ, Yoon JW, Cardoso RPR, Fontes Valente RA, Grácio JJ. On the use of a reduced enhanced solid-shell (RESS) element for sheet forming simulations. *International Journal of Plasticity* 2007; **23**(3):490–515.
48. Alves de Sousa RJ, Cardoso RPR, Fontes Valente RA, Yoon JW, Grácio JJ, Natal Jorge RM. A new one-point quadrature enhanced assumed strain (EAS) solid-shell element with multiple integration points along thickness – part II: nonlinear applications. *International Journal for Numerical Methods in Engineering* 2006; **67**(2):160–188.
49. Sze KY, Chan WK, Pian THH. An eight-node hybrid-stress solid-shell element for geometric non-linear analysis of elastic shells. *International Journal for Numerical Methods in Engineering* 2002; **55**(7):853–878.
50. Wempner G. Finite elements, finite rotations and small strains of flexible shells. *International Journal of Solids and Structures* 1969; **5**(2):117–154.
51. Belytschko T, Hsieh BJ. Non-linear transient finite element analysis with convected co-ordinates. *International Journal for Numerical Methods in Engineering* 1973; **7**(3):255–271.
52. Haugen B. Buckling and stability problems for thin shell structures using high performance finite elements. *Ph.D. Thesis*, Colorado At Boulder, 1994.
53. Jiang L, Chernuka MW. Simple four-noded corotational shell element for arbitrarily large rotations. *Computers and Structures* 1994; **53**(5):1123–1132.
54. Stolarski H, Belytschko T, Sang-Ho L. A review of shell finite elements and corotational theories. *Computational Mechanics Advances* 1995; **2**(2):125–212.
55. Battini JM. A modified corotational framework for triangular shell elements. *Computer Methods in Applied Mechanics and Engineering* 2007; **196**(13–16):1905–1914.
56. Crisfield MA, Moita GF. A co-rotational formulation for 2-D continua including incompatible modes. *International Journal for Numerical Methods in Engineering* 1996; **39**(15):2619–2633.
57. Moita GF, Crisfield MA. A finite element formulation for 3-D continua using the co-rotational technique. *International Journal for Numerical Methods in Engineering* 1996; **39**(22):3775–3792.
58. Felippa CA, Haugen B. A unified formulation of small-strain corotational finite elements: I. Theory. *Computer Methods in Applied Mechanics and Engineering* 2005; **194**(21–24 SPEC. ISS.):2285–2335.
59. Rankin CC, Brogan FA. An element independent corotational procedure for the treatment of large rotations. *Journal of Pressure Vessel Technology-Transactions of the ASME* 1986; **108**(2):165–174.
60. Nour-Omid B, Rankin CC. Finite rotation analysis and consistent linearization using projectors. *Computer Methods in Applied Mechanics and Engineering* 1991; **93**:353–384.
61. Rankin C. Application of linear finite elements to finite strain using corotation. *AIAA Paper 2006-1751, 47th AIAA Structures, Structural Dynamics and Materials Conference*, 2006.
62. Felippa CA. A study of optimal membrane triangles with drilling freedoms. *Computer Methods in Applied Mechanics and Engineering* 2003; **192**(16–18):2125–2168.
63. Sze K, Ghali A. Hybrid hexahedral element for solids, plates, shells and beams by selective scaling. *International Journal for Numerical Methods in Engineering* 1993; **36**(9):1519–1540.
64. Lee S, Pian T. Improvement of plate and shell finite elements by mixed formulations. *AIAA Journal* 1978; **16**(1):29–34.
65. Lee S, Wong S. Mixed formulation finite elements for mindlin theory plate bending. *International Journal for Numerical Methods in Engineering* 1982; **18**(9):1297–1311.
66. Pian THH, Sumihara K. Rational approach for assumed stress finite elements. *International Journal for Numerical Methods in Engineering* 1984; **20**(9):1685–1695.
67. Felippa CA. Supernatural QUAD4: a template formulation. *Computer Methods in Applied Mechanics and Engineering* 2006; **195**(41–43):5316–5342.
68. Mostafa M, Sivaselvan MV, Felippa CA. Reusing linear finite elements in material and geometrically nonlinear analyses—application in plane stress problems. *Finite Elements in Analysis and Design* 2013; **69**:62–72.
69. Fraeijs de Veubeke B. The dynamics of flexible bodies. *International Journal of Engineering Science* 1976; **14**(10):895–913.
70. Belytschko T, Bindeman LP. Assumed strain stabilization of the eight node hexahedral element. *Computer Methods in Applied Mechanics and Engineering* 1993; **105**(2):225–260.
71. Kasper EP, Taylor RL. A mixed-enhanced strain method. I. Geometrically linear problems. *Computers and Structures* 2000; **75**(3):237–250.

72. Reese S. A large deformation solid-shell concept based on reduced integration with hourglass stabilization. *International Journal for Numerical Methods in Engineering* 2007; **69**(8):1671–1716.
73. Alves de Sousa RJ, Cardoso RPR, Fontes Valente RA, Yoon JW, Grácio JJ, Natal Jorge RM. A new one-point quadrature enhanced assumed strain (EAS) solid-shell element with multiple integration points along thickness: part 1—Geometrically linear applications. *International Journal for Numerical Methods in Engineering* 2005; **62**(7):952–977.
74. ABAQUS. ABAQUS theory and manuals, 2010.
75. Cardoso RPR, Yoon JW. One point quadrature shell elements: a study on convergence and patch tests. *Computational Mechanics* 2007; **40**(5):871–883.
76. Gruttmann F, Wagner W. A linear quadrilateral shell element with fast stiffness computation. *Computer Methods in Applied Mechanics and Engineering* 2005; **194**(39–41):4279–4300.
77. Cardoso RPR, Yoon JW, Fontes Valente RA. A new approach to reduce membrane and transverse shear locking for one-point quadrature shell elements: linear formulation. *International Journal for Numerical Methods in Engineering* 2005; **66**(2):214–249.
78. Cardoso RPR, Yoon JW, Grácio JJ, Barlat F, César de Sá JMA. Development of a one point quadrature shell element for nonlinear applications with contact and anisotropy. *Computer Methods in Applied Mechanics and Engineering* 2002; **191**(45):5177–5206.
79. Bischoff M, Ramm E. Shear deformable shell elements for large strains and rotations. *International Journal for Numerical Methods in Engineering* 1997; **40**(23):4427–4449.
80. Parisch H. An investigation of a finite rotation four node assumed strain shell element. *International Journal for Numerical Methods in Engineering* 1991; **31**:127–150.
81. Stander N, Matzenmiller A, Ramm E. Assessment of assumed strain methods in finite rotation shell analysis. *Engineering Computations* 1989; **6**(1):58–66.
82. Bathe KJ, Wilson EL. *Numerical Methods in Finite Element Analysis*. Prentice-Hall: Englewood Cliffs, N.J., 1976.
83. Hughes TJR. *The Finite Element Method: Linear Static and Dynamic Finite Element Analysis*. Dover Publications: Mineola, NY, 2000.
84. Taylor RL, Simo JC, Zienkiewicz OC, Chan ACH. The patch test – a condition for assessing FEM convergence. *International Journal for Numerical Methods in Engineering* 1986; **22**(1):39–62.
85. Zienkiewicz OC, Taylor RL. The finite element patch test revisited. A computer test for convergence, validation and error estimates. *Computer Methods in Applied Mechanics and Engineering* 1997; **149**:223–254.
86. MacNeal RH, Harder RL. Proposed standard set of problems to test finite element accuracy. *Finite Elements in Analysis and Design* 1985; **1**(1):3–20.
87. Belytschko T, Liu WK. Test problems and anomalies in shell finite elements. *Proceedings of the International Conference on Reliability of Methods for Engineering Analysis*, Pineridge Press: Swansea, UK, 1986; 393–406.
88. Scordelis AC, Lo KS. Computer analysis of cylindrical shells. *American Concrete Institute – Journal* 1964; **61**(5):539–561.
89. Timoshenko S, Woinowsky-Krieger S. *Theory of Plates and Shells*, (2 edn.) McGraw-Hill: New York, 1959.
90. Cook R, Malkus D, Plesha M. *Concepts and Applications of Finite Element Analysis*, (3 edn.) John Wiley and Sons: New York, 1989.
91. Riks E. The application of Newton's method to the problem of elastic stability. *Journal of Applied Mechanics-Transactions of the ASME. Series E* 1972; **39**(4):1060–1065.
92. Fried I. Orthogonal trajectory accession to the nonlinear equilibrium curve. *Computer Methods in Applied Mechanics and Engineering* 1984; **47**(3):283–297.
93. Timoshenko S, Gere J. *Theory of Elastic Stability*, Vol. 2nd. MacGraw-Hill: New York, 1963.
94. Han SC, Kim KD, Kanok-Nukulchai W. An element-based 9-node resultant shell element for large deformation analysis of laminated composite plates and shells. *Structural Engineering and Mechanics* 2004; **18**(6):807–829.
95. Sze KY, Liu XH, Lo SH. Popular benchmark problems for geometric nonlinear analysis of shells. *Finite Elements in Analysis and Design* 2004; **40**(11):1551–1569.
96. Klinkel S, Wagner W. Geometrical non-linear brick element based on the EAS-method. *International Journal for Numerical Methods in Engineering* 1997; **40**(24):4529–4545.
97. Smolenski WM. Statically and kinematically exact nonlinear theory of rods and its numerical verification. *Computer Methods in Applied Mechanics and Engineering* 1999; **178**(1–2):89–113.
98. Basar Y, Ding Y. Finite-rotation elements for the non-linear analysis of thin shell structures. *International Journal of Solids and Structures* 1990; **26**(1):83–97.
99. Basar Y, Ding Y. Finite-rotation shell elements for the analysis of finite-rotation shell problems. *International Journal for Numerical Methods in Engineering* 1992; **34**(1):165–169.
100. Legay A, Combescure A. Elastoplastic stability analysis of shells using the physically stabilized finite element SHB8PS. *International Journal for Numerical Methods in Engineering* 2003; **57**(9):1299–1322.
101. Simo JC, Rifai MS. Class of mixed assumed strain methods and the method of incompatible modes. *International Journal for Numerical Methods in Engineering* 1990; **29**(8):1595–1638.